

Opposing trends in the peak and low ozone concentrations in eastern

China: Anthropogenic and meteorological influences

Zhuang Wang^{1,2}, Chune Shi^{1,2}, Hao Zhang^{1,2}, Xianguang Ji⁸, Yizhi Zhu⁷, Congzi Xia¹⁰, Xiaoyun Sun^{1,2},
Xinfeng Lin², Shaowei Yan², Suyao Wang⁹, Yuan Zhou^{11,12}, Chengzhi Xing^{3*}, Yujia Chen^{1,2*}, Cheng
Liu^{4,3,5,6*}

¹Anhui Province Key Laboratory of Atmospheric Science and Satellite Remote Sensing, Anhui Institute of Meteorological Sciences, Hefei 230031, China

²Shouxian National Climatology Observatory, Huaihe River Basin Typical Farm Eco–meteorological Experiment Field of CMA, Shouxian 232200, China

³Key Lab of Environmental Optics and Technology, Anhui Institute of Optics and Fine Mechanics, Hefei Institutes of Physical Science, Chinese Academy of Sciences, Hefei 230031, China

⁴Department of Precision Machinery and Precision Instrumentation, University of Science and Technology of China, Hefei, 230026, China.

⁵Center for Excellence in Regional Atmospheric Environment, Institute of Urban Environment, Chinese Academy of Sciences, Xiamen 361021, China

⁶Key Laboratory of Precision Scientific Instrumentation of Anhui Higher Education Institutes, University of Science and Technology of China, Hefei, 230026, China.

⁷School of Environmental Science and Engineering, Suzhou University of Science and Technology, Suzhou 215009, China

⁸Information Materials and Intelligent Sensing Laboratory of Anhui Province, Anhui University, Hefei 230601, China

⁹Huaibei Meteorological Bureau, Huaibei 235000, Anhui, China

¹⁰Institute of Big Data for Vocational Education, Guangdong Polytechnic of Science and Technology, Zhuhai 519000, China

¹¹Jiangxi Ecological Meteorology Center, Nanchang 330096, China

¹²Nanchang National Climate Observatory, Nanchang 330043, China

Correspondence to: Chengzhi Xing (xingcz@aiofm.ac.cn), Yujia Chen (chenyj18@mail.ustc.edu.cn), Cheng Liu (chliu81@ustc.edu.cn)

Abstract. Due to considerable reductions in nitrogen oxides (NO_x), ozone trends and variations in eastern China remain inadequately understood. Long-term observations of ozone precursors were conducted to explore the factors influencing ozone trends in this region. Combined with satellite and surface measurements, we evaluated the trends in low (2nd percentile), typical (50th percentile), and peak (98th percentile) ozone concentrations in detail. Observations indicate a significant decrease in peak ozone concentrations (-0.5% per year), alongside an increase in low ozone concentrations (0.3% per year) across eastern China during May–September from 2017 to 2022. The decline in typical ozone concentrations is notably slower than that of peak ozone concentrations, approximately -0.02 ppb/year (-0.0% per year) during the same period. Anthropogenic emissions primarily drive trends in low and peak ozone concentrations in eastern China, though meteorological effects also play a role. Ozone formation sensitivity shifts from VOC-limited or transitional regimes in the morning (8:00–11:00), when ozone

concentrations rise sharply, to NO_x-limited regimes around peak concentrations (~14:00). The reduction in NO_x concentrations is identified as a key factor driving the decline in peak ozone concentrations, aiming to further reduce ozone exceedance days. Thus, controlling NO_x concentrations emerges as crucial for mitigating peak ozone levels. Moreover, the increase in low ozone concentrations can also be attributed to both anthropogenic emissions and meteorological factors. Our findings underscore the beneficial impacts of NO_x reduction on managing peak ozone levels. Regular changes in ozone formation sensitivity throughout the day should be considered when formulating effective ozone control policies.

1 Introduction

In recent decades, China's rapid industrialization and urbanization have yielded substantial economic benefits but have also brought about serious environmental challenges (Li et al., 2018; Song et al., 2023; Wang et al., 2023c). Air pollutants, notably ozone (O₃, in warm seasons) and fine particulate matter (PM_{2.5}, in cold seasons), have been primary targets of China's air quality improvement efforts (Zhang and Cao, 2015; Xing et al., 2024; Xing et al., 2022; Wang et al., 2020; Bauwens et al., 2022). To combat this severe air pollution, the Chinese government initiated the Clean Air Action Plan in 2013 (State Council of China, 2013), resulting in significant reductions in most air pollutant concentrations. PM_{2.5} annual average concentrations were reduced by 30% to 50% from 2013 to 2018 (Zhai et al., 2019), while nitrogen oxides (NO_x) and carbon monoxide (CO) emissions dropped by 21% and 23%, respectively, from 2013 to 2017 (Zheng et al., 2018). However, O₃ concentrations showed a yearly increase of $3.3 \pm 4.7 \mu\text{g}/\text{m}^3/\text{year}$ from 2015 to 2019 (Mousavinezhad et al., 2021). Subsequently, the second phase of the Clean Air Action Plan was launched in 2018 (State Council of China, 2018), focusing on additional controls for O₃ emissions. Driven by both anthropogenic activities and meteorological patterns, the upward trend in O₃ levels in eastern China persisted through at least 2019 (Li et al., 2020a), making the study of O₃ formation, sources, and trends in densely populated areas a topic of increasing global concern (Wang et al., 2023a).

Ozone forms rapidly in polluted air through the photochemical oxidation of volatile organic compounds (VOCs) in the presence of NO_x (NO_x = NO + NO₂) (Li et al., 2022; Cooper et al., 2012). Ambient O₃ concentrations are influenced by various factors, including precursor levels (Wang et al., 2022b; Ding et al., 2023), local meteorological conditions (Han et al., 2020), regional transport (Lang et al., 2021; Wang et al., 2023b), and deposition (Wu et al., 2023). Elevated O₃ levels can have significant impacts on human health, ecosystems, and climate change, leading to substantial economic losses (Guan et al., 2021; Gao et al., 2022). The formation sensitivity of O₃ (VOC-limited, transition, and NO_x-limited regimes) in a region depends on the relative abundance of VOCs and NO_x and their competition for OH radicals, highlighting the importance of controlling both VOCs and NO_x to manage O₃ production and removal effectively (Ren et al., 2022b). While NO_x concentrations have significantly declined in eastern China since 2013 (Lin et al., 2019), anthropogenic VOC emissions continued to increase until 2019 (Zheng et al., 2018; Bauwens et al., 2022).

Numerous studies have investigated the drivers of the increasing O₃ trend in China over the past decade, particularly from 2013 to 2017 (Li et al., 2020a; Lu et al., 2020; Liu et al., 2023). Changes in meteorological conditions and anthropogenic

emissions have been identified as the primary causes, with both observations and models concluding that anthropogenic impacts dominate the increasing trend of summer O₃ in China. For instance, Li et al. (2020a) found that the increase in surface O₃ in the North China Plain (NCP) from 2013 to 2019 was more influenced by changes in emissions (1.2 ppb/year) than meteorological changes (0.7 ppb/year). Additionally, the decrease in PM_{2.5}, mainly achieved by reducing the scavenging of hydroxyl (HO₂) radicals on the aerosol surface, has been found to be crucial for the increase in O₃ (Li et al., 2018). However, the implications of the heterogeneous uptake of HO₂ radicals remain debated. These studies have largely focused on a single O₃ indicator, and due to the recent NO_x reduction, the reasons for the variations in O₃ trends in eastern China, particularly the low and peak O₃ trends, are not fully understood. This poses a significant challenge for controlling O₃ pollution and developing effective strategies for sustained air quality improvement.

This study aims to address two key issues by combining extensive ground-based and satellite observations: (1) to reveal the surface low, typical, and peak O₃ trends in eastern Chinese cities in recent years, and (2) to explore the driving forces behind these trends. First, we report long-term records of surface O₃ and related parameters observed at urban air quality monitoring sites and by satellites in eastern China, characterizing the trends of low, typical, and peak surface O₃ concentrations during the warm season (May–September) from 2017 to 2022. Then, a Multiple Linear Regression (MLR) model is used to evaluate the anthropogenic and meteorological contributions to the 98th and 2nd O₃ percentile trends. Next, secondary formaldehyde (HCHO) and NO₂ are employed to diagnose the diurnal variations in O₃ formation sensitivity and investigate the reasons for peak O₃ concentration trends in the context of current NO_x reduction. Finally, we discuss the reasons for the potential increase in low O₃ concentrations and the sensitivity of peak and low O₃ trends during the study period.

2 Materials and methodology

2.1 Surface measurements

The densely populated areas in eastern China mainly include the NCP and the Middle and Lower Yangtze River Plain (MLYRP), which are both vast and economically developed. It is one of the most polluted areas in China (Mousavinezhad et al., 2021). In this study, O₃ trends in 105 cities in eastern China were investigated, the spatial distribution of 105 cities in eastern China is shown in Fig.1a. Real-time hourly observed urban O₃, NO₂, and CO concentrations in 105 cities in eastern China from 2017 to 2022 were obtained from the open website of Ministry of Ecology and Environment of China (MEE; <https://www.mee.gov.cn>; last access: January 7, 2024), archive at <https://quotsoft.net/air/> (last access: January 7, 2024). As of August 31, 2018, MEE reported concentrations in µg/m³ under standard conditions (273 K, 1013 hPa). The reference status changed to 298 K and 1013 hPa on September 1, 2018. To facilitate analysis of the long-term series, the mass concentrations (µg/m³) of O₃, NO₂, and CO at each site were converted to volume mixing ratios (VMRs, ppb) to eliminate the effect of these changes on trend calculations. Data quality control methods and the calculation of daily maximum 8-hour O₃ (MDA8 O₃) concentrations were implemented according to the statistical requirements of the Technical Regulations for Environmental Air

Quality Evaluation (Trial) (HJ633–2013). According to the Technical Regulations of China Ambient Air Quality Index (Trial) (HJ633–2012), an MDA8 O₃ concentration greater than 160 µg/m³ is defined as O₃ exceedance days, otherwise it is O₃ normal day. Note that all times mentioned in this study refer to local time.

2.2 MAX–DOAS measurements

5 Three typical cities in the 105 cities in the eastern China were selected to be representative to conduct Multi–Axis Differential Optical Absorption Spectroscopy (MAX–DOAS) observations, namely Hefei, Huaibei and Tai' an. First, the three cities are located at similar longitudes with large differences in latitude, transitioning sequentially from south to north (Fig. 1a). Secondly, the O₃ concentrations of the three cities differed greatly, with Tai' an having a higher surface mean MDA8 O₃ concentration (82.9 ppb), Hefei having a lower surface mean MDA8 O₃ concentration (65.5 ppb), and Huaibei having an
10 intermediate surface mean MDA8 O₃ concentration (74.3 ppb). The three observation stations in Hefei (31.827 °N, 117.233 °E), Huaibei (33.962 °N, 116.805 °E), and Tai' an (36.205 °N, 117.094 °E) are all set up in urban areas, and the observation periods were from 22 December, 2020, to 15 May 2023, 12 April, 2019, to 27 May 2022, and 15 July, 2021, to 15 May 2023, respectively.

The MAX–DOAS employed in this study consisted of a telescope, two spectrometers (UV: 303–370 nm; VIS: 390–550
15 nm, temperature stabilized at ~20 °C), and a computer as the control and data acquisition unit. The telescope elevation angles were set to 1–6, 8, 10, 15, 30, and 90° and controlled by stepper motors. MAX–DOAS measures spectral information to retrieve aerosols and trace gas profiles. The system was operated only during the daytime (08:00–17:00 local time) with a temporal resolution of 15 min and a spatial resolution of 100 m. Because this study focused on surface O₃ formation sensitivity, only the lowest level data of NO₂ and HCHO VMRs (ppb) were used. Detailed information regarding the MAX–DOAS instrument,
20 measurement procedures, data inversion algorithms, and data quality control can be found in previous studies (Liu et al., 2022b; Wang et al., 2020; Xing et al., 2022).

Ground–based MAX–DOAS and tropospheric monitoring instrument (TROPOMI) observations were compared to ensure reliability of the data used in this study. Because the satellite overpass was at approximately 13:30, the mean MAX–DOAS results between 13:00 and 14:00 were used for comparison. TROPOMI observations were averaged over a range of 0.2° from
25 the ground–based MAX–DOAS station. Comparisons of NO₂ and HCHO tropospheric vertical column densities (VCD) from the MAX–DOAS and TROPOMI observations are shown in Fig. S1 and S2. In general, the MAX–DOAS and TROPOMI observations were in good agreement. The Pearson correlation coefficient of monthly average NO₂ VCD is 0.99 (P<0.01), 0.96 (P<0.01) and 0.96 (P<0.01) in Hefei, Huaibei and Tai' an, respectively, and the Pearson correlation coefficient of monthly average HCHO VCD is 0.88 (P<0.01), 0.77 (P<0.01) and 0.68 (P<0.01) in Hefei, Huaibei and Tai' an, respectively. Generally,
30 the NO₂ and HCHO VCD observed by TROPOMI were smaller than those observed by MAX–DOAS, and the difference may be caused by fitting errors, a priori model bias, cloud and aerosols, and spatio–temporal resolution (De Smedt et al., 2021; Dimitropoulou et al., 2020). In addition, the bottom NO₂ concentrations observed by MAX–DOAS were also compared with

urban surface NO₂ concentrations measured by MEE (Fig.S3), and the results were also comparable to the comparisons reported in previous studies (Lin et al., 2022; Wang et al., 2020), with Pearson correlation coefficient of 0.74 (P<0.01), 0.66 (P<0.01), and 0.73 (P<0.01) for Hefei, Huaibei, and Tai'an, respectively. Thus, the MAX-DOAS data are reliable. The differences between MAX-DOAS and MEE observations arise from these two components. First, there was a difference in the detection geometries, as the urban NO₂ concentration observed by MAX-DOAS was the result of scanning along a certain direction, whereas the urban NO₂ concentration observed by MEE was sampled in situ. Second, there were some differences in their locations, and the urban NO₂ concentration of the MEE was the average of several in-situ observation stations (10, 3, and 3 in Hefei, Huaibei, and Tai'an, respectively), whereas we only used one MAX-DOAS in each city.

2.3 Satellite observations

TROPOMI is an imaging spectrometer onboard the European Space Agency's Copernicus Sentinel 5 Precursor satellite launched in October 2017 with a daily overpass of approximately 13:30. TROPOMI has a spatial resolution of 3.6 × 7.2 km (before 6 August 2019) and 3.6 × 5.6 km (after 6 August 2019). A more detailed description of TROPOMI can be found in Veeffkind et al. (2012). The TROPOMI NO₂ ("S5P_OFFL_L2_NO2...") and HCHO ("S5P_OFFL_L2_HCHO...") tropospheric VCD products during May-September 2018-2022, TROPOMI O₃ profiles ("S5P_OFFL_L2_O3_PR...") during May-September 2022 were used in this study (Download from <https://search.earthdata.nasa.gov/search>; last access: January 7, 2024) (Van Geffen et al., 2020; De Smedt et al., 2018). The recommended quality control (QC, in the range of 0-1) filter was applied to exclude HCHO and O₃ profiles retrieval values with QC marks less than 0.5, and NO₂ retrieval values with QC marks less than 0.75. In addition, the TROPOMI observed HCHO VCD and NO₂ VCD were regridded to 0.05×0.05° (approximately 5×5 km) in this study.

2.4 Stepwise Multiple Linear Regression Model

To quantify the importance of meteorological drivers, numerous previous studies have used stepwise MLR to derive the relationships between meteorological factors and observed surface O₃ concentrations in China (Liu et al., 2023; Li et al., 2020a; Li et al., 2018; Han et al., 2020; Zhang et al., 2023b). These studies demonstrated the importance of stepwise MLR in quantifying the contribution of meteorological and anthropogenic components to O₃ concentrations. We used the same stepwise MLR modeling approach as (Zhai et al., 2019; Li et al., 2018; Li et al., 2020a; Sun et al., 2022; Liu et al., 2023). Stepwise regressions were performed, adding and removing terms based on their independent statistical significance to obtain the best model fit. Daily meteorological variables were obtained from the ERA5 reanalysis data (Download from <https://cds.climate.copernicus.eu>, last access: January 7, 2024), included temperature (T, °C), surface relative humidity (RH, %), total cloud cover (TCC), total precipitation (TP, mm), mean sea level pressure (MSLP, hPa), wind speed of U, V

components (U, V, m/s), boundary layer height (BLH, m), and vertical velocity at 850 hPa (V850, m/s). Details of the meteorological parameters are presented in Table S1.

5 First, we used the MLR model to remove the effects of meteorological variability from the 2017 to 2022 98th or 2nd O₃ percentile trends. The meteorological anomalies X_k during May–September 2017–2022 was obtained by removing the 6–year means of the 50 d moving averages from the 10 d mean time series. The anomalies calculated in this process were deseasonalized but not detrended. This yields the meteorology–driven 98th or 2nd O₃ percentile anomalies $Y_m(t)$

$$Y_m(t) = R + \sum_{k=1}^n \beta_k X_k(t) \quad (1)$$

10 Where R is the regression constant, β_k is the regression coefficient. Secondly, to avoid overfitting, only the three most important meteorological parameters were selected based on their individual contributions to the regressed 98th or 2nd O₃ percentiles, along with the requirement that they be statistically significant above the 95% confidence level in the MLR model (Li et al., 2018). The fit results and selected meteorological variables varied by city but were regionally consistent (Table S2 and Table S3). The 98th or 2nd O₃ percentile anomalies $Y_a(t)$ obtained by deseasonalizing, but not detrending, the 98th or 2nd O₃ percentile time series in a similar manner as for the meteorological variables (by removing the 6–year means of the 50 d moving averages). The residual anomaly $Y_r(t)$ after removing the meteorology–driven 98th or 2nd O₃ percentile anomalies
15 from the MLR model is given by

$$Y_r(t) = Y_a(t) - Y_m(t) \quad (2)$$

Finally, the residual is an anomalous component that cannot be explained by the MLR meteorological model and is referred to as meteorologically corrected data by Zhai et al. (2019). It consists of noise due to the limitations of the MLR model and other factors and can be mainly attributed to long–term trends in anthropogenic emission changes over a 6–year period.
20 The trend in the regressed 98th or 2nd O₃ percentile reflected the meteorological contribution, and the residual was then used to reflect the presumed anthropogenic contribution.

2.5 Regression Model for source separation in primary and secondary HCHO

Tracer–driven linear regression models have been widely used to separate primary and secondary sources of HCHO (Lin et al., 2022; Sun et al., 2021; Hong et al., 2018; Liu et al., 2024; Bao et al., 2022; Heue et al., 2014; Macdonald et al., 2012).
25 CO is emitted directly into the atmosphere through combustion processes (e.g., incomplete combustion in vehicle engines) and can be used as a tracer for primary HCHO emissions (Garcia et al., 2006). O₃ reacts with NO emitted from automobiles to form NO₂. Therefore, odd amounts of oxygen (O_x = O₃ + NO₂) are often used as tracers of photochemical processes in urban atmospheres (Wood et al., 2010). In this study, CO and O_x were selected as tracers to separate the primary and secondary sources of ambient HCHO, as expressed in Eq. 3:

$$[HCHO] = \beta_0 + \beta_1 \times [CO] + \beta_2 \times [O_x] \quad (3)$$

Where β_0 , β_1 , and β_2 are regression coefficients. where [HCHO], [CO], and [O_x] are the ambient HCHO, CO, and O_x VMRs, respectively.

The relative contributions of the primary, secondary, and atmospheric background HCHO to the total ambient HCHO were calculated from the tracer VMRs and the corresponding regression coefficients:

$$P_{bg} = \frac{\beta_0}{\beta_0 + \beta_1 \times [CO] + \beta_2 \times [O_x]} \times 100\% \quad (4)$$

$$P_{pri} = \frac{\beta_1 \times [CO]}{\beta_0 + \beta_1 \times [CO] + \beta_2 \times [O_x]} \times 100\% \quad (5)$$

$$P_{sec} = \frac{\beta_2 \times [O_x]}{\beta_0 + \beta_1 \times [CO] + \beta_2 \times [O_x]} \times 100\% \quad (6)$$

Where P_{pri} denotes the contribution of primary sources of HCHO (e.g., vehicular and industrial emissions), P_{sec} denotes the contribution of secondary sources of HCHO (photochemical oxidation), and P_{bg} denotes the background HCHO. According to previous studies in Central and Eastern China (Ma et al., 2016; Wang et al., 2015), the background level of HCHO was limited to 1 ppb. Therefore, the regression parameter β_0 was fixed at 1 ppb in this study (Hong et al., 2018; Lin et al., 2022). We first perform hourly averaging of HCHO data from MAX–DOAS observations to match CO and O_x data from MEE observations. Primary and secondary HCHO will then be separated for all available HCHO data from May to September in the MAX–DOAS measurement period. The fitted parameters of the MLR for the measured and modelled HCHO are shown in Fig.S4, it is comparable to the comparisons reported in previous studies (Lin et al., 2022; Sun et al., 2021). As other factors (e.g., meteorological conditions) can also affect the atmospheric HCHO concentration, regression models are difficult to obtain very consistent results.

3 Results and discussions

3.1 Trends of O₃ and its precursors in eastern China

Figure 1 presents the spatial distribution of the surface mean MDA8 O₃ VMRs at all available urban sites (105 cities in total) in eastern China during May–September of 2017–2022. High MDA8 O₃ VMRs were concentrated in the western cities of eastern China, with the highest values in Jiaozuo, up to 86.4 ppb. High O₃ VMRs indicate intensive anthropogenic emissions of O₃ precursors from these cities, most of which are located in the NCP, one of the most polluted areas in China (Li et al., 2018). Fig. 1b and c show the average VCDs of NO₂ and HCHO observed by TROPOMI during May–September 2018–2022, respectively. High NO₂ and HCHO levels were clustered mainly in the NCP and MLYRP. In this study, the 2nd, 50th, and 98th

percentiles of the hourly O₃ and NO₂ concentrations for cities in eastern China were calculated to determine long-term trends at low, typical, and peak concentration levels, respectively (Cooper et al., 2012; Li et al., 2022; Gaudel et al., 2020). Different percentiles may be related to different influences, such as background concentration levels, emission changes, climate change, and regional transport effects (Lefohn et al., 2010). Li et al. (2014) reported that concentrations below the 5th, between 25th and 75th, and above 95th represent background, typical, and polluted concentrations, respectively. In principle, the lowest daily O₃ concentrations usually occur before sunrise due to nighttime titration of NO, and the low percentile (2nd) usually characterizes baseline or background conditions because increases in the low O₃ percentile tend to be associated with increases in baseline or background O₃ concentrations. Similar conclusions were also obtained from both models and observations (Jacob et al., 1999; Cynthia Lin et al., 2000). O₃ pollution in eastern China generally occurs in the late afternoon on clear days in the warm season (Wang et al., 2022a), when the ambient O₃ concentration is highest, so the high percentile (98th) characterizes the conditions of the pollution events. The middle percentiles (25th, 50th and 75th) usually follow the same trend as the mean values and therefore represent typical conditions (Cooper et al., 2012; Li et al., 2022). Using these indicators to investigate long-term changes in O₃ and NO₂ helps gain a more detailed understanding through analyses.

As shown in Fig.2, the 98th O₃ percentile in eastern China showed a significant decreasing trend (about -0.39 ppb/year, -0.5% per year) during May–September 2017–2022, and the corresponding O₃ exceedance days (-1.1% per year) and exceedance hours (-1.6% per year) are also dropped. This is in stark contrast to previous studies, which have widely observed a rapid increase in average surface O₃ concentrations in Chinese cities, while ignoring changes in their peak concentrations (Lu et al., 2020; Liu et al., 2023; Li et al., 2018; Li et al., 2021; Chan et al., 2017). The decline rate of 50th O₃ percentile is considerably slower than that of 98th O₃ percentile during May–September 2017–2022, about -0.02 ppb/year (-0.0% per year). Unexpectedly, the 2nd O₃ percentile in eastern China showed an increasing trend (about 0.06 ppb/year, 0.3% per year) during May–September 2017–2022, the increase in 2nd O₃ concentrations may be due to the decrease in O₃ titration from fresh NO emissions as NO_x emissions decrease (Li et al., 2023). It can be confirmed in Fig. 2b that all the three NO₂ percentiles (2nd, 50th, and 98th) show a significant decreasing trend during May–September 2017–2022, with relative decreasing trends of -2.1%, -1.8%, and -1.8% per year, respectively. Notably, NO₂ declines more rapidly in 2020 and 2021, mainly because of the impact of the COVID–19 pandemic, which has been discussed in detail in previous studies (Liu et al., 2022a). Satellite observations also found a significant decrease in NO₂ concentration in eastern China (Fig.3a), with a decrease rate of about $0.09 \times 10^{15} \text{ mol/cm}^2/\text{year}$ (-1.8% per year). Since 2013, there have decreased in NO_x emissions in China owing to a series of air pollution prevention and control policies (Lin et al., 2019; Wang et al., 2019).

We further examined the trends in the 98th and 2nd O₃ percentiles across cities in eastern China from May to September 2017–2022 (Fig. 4). Generally, the trend in low O₃ concentrations in most cities showed an increase, with the 2nd O₃ percentile ranging from -0.2 to 0.5 ppb/year (-1.6–5.6% per year). Conversely, peak O₃ concentrations exhibited a decreasing trend, with the 98th O₃ percentile ranging from -1.1 to 0.2 ppb/year (-1.0–0.3% per year). The trend in typical O₃ concentrations in eastern

China from May to September 2017–2022 ranging from -0.4 to 0.3 ppb/year (-0.8–0.8% per year), with about one third of the cities increasing and two thirds decreasing. The decline in peak O₃ concentrations and the rise in low O₃ concentrations were notably more pronounced in the NCP compared to the MLYRP. The highest increase in low O₃ concentrations was observed in Handan at 0.5 ppb/year, while the lowest decrease in peak O₃ concentrations was seen in Baoding at 1.1 ppb/year. Additionally, we investigated the relationship between the trend in mean NO₂ concentrations and the trend in the 98th O₃ percentiles from May to September 2017–2022, revealing a significant positive correlation with a Pearson correlation coefficient of R=0.42 (P<0.01; Fig. 5). In contrast, the trend in the 98th NO₂ percentile during the same period showed a significant negative correlation with the trend in the 2nd O₃ percentiles, with a Pearson correlation coefficient of R=-0.41 (P<0.01). Therefore, the substantial reduction in NO_x emissions may have had divergent impacts on low and peak O₃ levels, contributing to the observed decrease in low O₃ concentrations and increase in peak O₃ concentrations across urban areas in eastern China.

Due to the absence of long-term ground-based VOCs observations, satellite-observed HCHO VCD were utilized to indicate VOCs variations in eastern China from May to September 2018–2022. HCHO is a transient product reflecting the oxidation of various VOCs, serving as a proxy for VOCs emissions, as used in previous studies (Zheng et al., 2018; Zhang et al., 2019). The TROPOMI satellite observations showed a significant upward trend in HCHO VCD in eastern China during May–September from 2018 to 2022, approximately $0.11 \times 10^{15} \text{ mol/cm}^2/\text{year}$ (0.7% per year) (Fig. 3b). Generally, HCHO VCD exhibits seasonal variability (Li et al., 2021), with higher temperatures and sufficient radiation enhancing photochemical reactions of VOCs and biogenic VOC emissions, thereby promoting HCHO formation (Ren et al., 2022b). In China, anthropogenic VOCs emissions continued to increase until 2019 (Zheng et al., 2018), after which measures were implemented to control them. However, biogenic VOC emissions have been rising in recent years, particularly during extreme heat events such as those experienced in the MLYRP in 2022, leading to a significant increase in biogenic VOCs emissions (Zhang et al., 2022; Zhang et al., 2023a). Importantly, reductions in anthropogenic VOCs have not been sufficient to offset the overall increasing trend in VOCs emissions across eastern China (Li et al., 2020b).

3.2 Anthropogenic and meteorological contributions to O₃ trends

The MLR model was applied to assess the significance of the anthropogenic and meteorological components on the 98th and 2nd O₃ percentile trends. It is worth noting that the aim of this section is not to accurately assess the contribution of each meteorological factor and precursor concentration to O₃ trends but to explore trends in the 98th and 2nd O₃ percentile concentrations due to variations in meteorological conditions and anthropogenic emissions in eastern China and to determine the magnitude of the 98th and 2nd O₃ percentile trends. Based on the daily output of the MLR model, the monthly mean meteorological and anthropogenic components of the 98th and 2nd O₃ percentiles from May to September 2017–2022 were calculated, and the relative contributions of the meteorological and anthropogenic components to the 98th and 2nd O₃ percentile trends were quantified. Based on the MLR model, the three key meteorological factors with the most significant effects on the

98th and 2nd O₃ percentiles were selected (Li et al., 2018; Li et al., 2020a). The meteorological components of the 98th and 2nd O₃ percentile concentrations were then simulated using the MLR model driven by the three selected key meteorological factors, and the coefficients of each factor and the Pearson correlation coefficients (R) of the fitted MLR model were obtained. The R for each city of eastern China was in the range of 0.16 to 0.77 for 2nd O₃ percentiles (Table S2) and 0.24 to 0.84 for 98th O₃ percentiles (Table S3), respectively. RH and T were the most important factors affecting the 98th and 2nd O₃ percentile concentrations, followed by TCC, BLH, U, V, and V850 (Tables S2 and S3). These results are consistent with the current understanding of the meteorological effects of O₃ (Weng et al., 2022; Li et al., 2020a; Ding et al., 2023).

Figure 6 shows the trends in the monthly mean observed 98th and 2nd O₃ percentile concentrations, meteorological 98th and 2nd O₃ percentile components in the MLR simulations, and the residual anthropogenic 98th and 2nd O₃ percentile components during May–September 2017–2022. The trend of the monthly mean 98th O₃ percentile meteorological component obtained by the MLR model from May to September 2017–2022 was considerably smaller than that of the anthropogenic component, with almost no trend between 2017 and 2022 (0.005 ppb/year). Meteorological influences explained only 3% (0.005 ppb/year) of the observed 98th O₃ percentile trend during May–September 2017–2022, with the remaining -103% (-0.183 ppb/year) determined by anthropogenic influences. However, if we count the monthly mean 98th O₃ percentiles trends from May–September 2017–2021, we find a more significant downward trend in 98th O₃ percentiles (-0.363 ppb/year), with a contribution of -0.119 ppb/year (-33%) from the meteorological component and -0.244 ppb/year (-67%) from the anthropogenic component (Table 1). The differences in the O₃ trend statistics for 2017–2022 and 2017–2021 are mainly due to the meteorological conditions in 2022, which will be analyzed in detail in the discussion section. Separating the observed 2017–2022 98th O₃ percentiles trends by month shows that the seasonal May–September trend of -0.178 ppb/year over eastern China (Table 1) is driven by June, July and September. The observed trends were -0.020 ppb/year for May, -4.437 ppb/year for June, -1.745 ppb/year for July, -0.687 ppb/year for August, and 1.999 ppb/year for September. This month-to-month difference was driven mainly by meteorology. As derived from the MLR model, the meteorologically driven 98th O₃ percentile trends for July and September were -1.100 and 1.136 ppb/year, respectively, which are larger than those of the anthropogenic trend (-0.645 ppb/year for July and 0.863 ppb/year for September).

The trend of the mean 2nd O₃ percentiles meteorological component (0.008 ppb/year, 7.0%) was also smaller than that of the anthropogenic component (0.107 ppb/year, 93.0%) from May–September 2017–2022. It is worth noting that the increasing trend of 2nd O₃ percentiles during May–September 2017–2021 was significantly smaller than that during May–September 2017–2022 (0.027 vs. 0.115 ppb/year). The contribution of meteorological components to 2nd O₃ percentile trends during May–September 2017–2021 was -0.044 ppb/year (-163.0%), while the anthropogenic component trend of 2nd O₃ percentiles was 0.071 ppb/year (263.0%) (Table 1). This indicates that meteorological factors are not conducive to the increasing trend of low O₃ concentrations during May–September 2017–2021, and that the increasing trend of low O₃ concentration is mainly controlled by anthropogenic influences. In addition, the observed 2017–2022 2nd O₃ percentile trend by month was 0.322 ppb/year in May, 0.205 ppb/year in June, 0.768 ppb/year in July, 0.371 ppb/year in August, and 1.290 ppb/year in September. The observed 2017–2022 2nd O₃ percentile trends by month were driven by July and September, while

the sign of the 2nd O₃ percentile trends, driven by meteorological and anthropogenic components, was reversed in July (-0.177 vs. 0.945). Therefore, although anthropogenic emissions are the main driver of opposing trends in peak and low O₃ concentrations in eastern China, the effect of changes in meteorological components on the 2nd and 98th O₃ percentile trends cannot be ignored.

5 3.3 Diurnal differences in surface O₃ formation sensitivity

To elucidate the reasons for changes in peak, typical, and low O₃ concentrations in the presence of emission reductions in O₃ precursors (a substantial decrease in NO_x emissions and a slight increase in VOCs emissions), it is critical to accurately determine the O₃ formation sensitivity to its precursors, especially at a high temporal resolution. Secondary HCHO and NO₂ were selected as the representative VOCs and NO_x respectively (Xue et al., 2022; Hong et al., 2022; Hong et al., 2018; Lin et al., 2022; Ren et al., 2022a). Surface NO₂ and HCHO VMRs retrieved from ground-based MAX-DOAS observations were used to diagnose the surface O₃ formation-sensitive regime. The thresholds for the VOC-limited, transition, and NO_x-limited regimes were determined based on the correlation between the O₃ concentrations and the changes in O₃ precursor concentrations under different FNR (defined as the ratio of HCHO VMRs to NO₂ VMRs; $FNR = HCHO/NO_2$). Here, we used FNR_{sec} (defined as the ratio of secondary HCHO to NO₂; $FNR_{sec} = HCHO_{sec}/NO_2$) as an indicator of O₃ formation sensitivity.

Compared with conventional FNR, FNR_{sec} eliminate background and primary HCHO interference, improve the accuracy of diagnosing O₃ formation sensitivity, and contribute to a better understanding of O₃ formation sensitivity (Lin et al., 2022; Xue et al., 2022). Most of FNR_{sec} values (~98%) varied between 0.03~1.5 during the whole observations, and excessively low FNR_{sec} values can be attributed to deficiencies in the HCHO source assignment in the MLR model. Therefore, FNR_{sec} values greater than 1.5 or less to 0.03 were filtered out for quality control.

Three steps are involved in determining the FNR_{sec} threshold. First, the surface-hourly averaged secondary HCHO and NO₂ VMRs during May–September based on MAX-DOAS observations were normalized by dividing their respective mean values because of the large differences in surface HCHO and NO₂ concentrations (Su et al., 2017; Ren et al., 2022a). The ratio of the hourly averaged O₃ VMRs to the hourly averaged normalized NO₂ VMRs (S_{NO_2}) and the ratio of the hourly averaged O₃ VMRs to the hourly averaged normalized secondary HCHO VMRs (S_{HCHO}) were calculated. Finally, third-order polynomials were used to fit S_{NO_2} and S_{HCHO} (Fig.7).

As shown in Fig.7, the third-order fitting of S_{NO_2} increased almost linearly with the FNR_{sec} values, similar to S_{HCHO} . When S_{NO_2} is significantly larger than S_{HCHO} , O₃ formation is more sensitive to NO_x, which is the NO_x-limited regime, and vice versa. For example, in Hefei, S_{NO_2} and S_{HCHO} intersected at FNR_{sec}=0.21. FNR_{sec} less than 0.16 and greater than 0.29 correspond to VOC-limited regime and NO_x-limited regime, respectively, where the relative difference between S_{NO_2} and S_{HCHO} is more than 25% (Lin et al., 2022), and the range of FNR_{sec} from 0.16 to 0.29 represents a transition regime. For Huaibei and Tai'an, the transition regime range was 0.24–0.44 and 0.14–0.24, respectively. The FNR_{sec} threshold for O₃ formation sensitivity varies in different cities, which may be due to differences in O₃ precursor emissions.

Figure 8 shows the diurnal variations in O_3 and its precursors at three stations (Hefei, Huaibei, and Tai'an) in eastern China, from south to north. O_3 and NO_2 VMRs showed diametrically opposite trends from 08:00 to 13:00, with O_3 concentrations rapidly increasing (about 8.2, 7.4, and 8.6 ppb/hour in Hefei, Huaibei, and Tai'an, respectively) and NO_2 concentrations gradually decreasing (about -0.90, -0.86, and -1.49 ppb/hour in Hefei, Huaibei, and Tai'an, respectively).

5 Ambient HCHO concentrations depend on the primary emissions and photo-oxidation of VOCs (Xue et al., 2022). We separated the primary and secondary sources of HCHO using the CO and O_x VMRs, and their diurnal variations are shown in Fig.8 d–f. The primary source contributed the most to ambient HCHO concentration. Atmospheric primary HCHO concentrations are mainly derived from motor vehicle exhaust, petrochemical industry, solvent use, and combustion emissions (Ma et al., 2019). Hefei, Huaibei, and Tai'an are located in the NCP, which is the region with the highest primary emissions of air pollutants in China (Li et al., 2017). The rapid industrialization and urbanization in these developing cities has influenced the primary and secondary HCHO concentrations, and HCHO mainly stems from initial atmospheric pollutants (Lu et al., 2024). The HCHO from primary emissions was highest between 08:00 and 10:00 (about 2.63, 2.50, and 4.30 ppb in Hefei, Huaibei, and Tai'an, respectively), then gradually decreased, reaching the lowest concentration around 15:00, about 1.78, 1.54, and 1.82 ppb in Hefei, Huaibei, and Tai'an, respectively, and then gradually rising. High primary HCHO concentrations in the morning and evening may have been due to emissions from traffic (Hong et al., 2018; Zhang and Cao, 2015). Secondary HCHO concentrations were lowest in the morning, about 0.58, 0.84, and 0.65 ppb in Hefei, Huaibei, and Tai'an, respectively, with the enhancement of photochemical reactions and the resumption of human activities, the secondary HCHO concentrations gradually increased from 08:00 to 12:00, and the first peak usually occurred at 11:00–14:00. The proportion of secondary HCHO VMRs in the total HCHO VMRs also increased rapidly, and the proportion of secondary HCHO VMRs in the total HCHO VMRs gradually stabilized after 12:00, about 24%, 31%, and 22% in Hefei, Huaibei, and Tai'an, respectively. Similar diurnal variation trends were found in Shenyang (Xue et al., 2022), Nanjing (Hong et al., 2018), Guangzhou (Lin et al., 2022), Shenzhen (Zhang and Cao, 2015), Rome (Possanzini et al., 2002) and Toyama (Taguchi et al., 2020), etc. It is worth noting that the secondary HCHO VMRs in Hefei, Huaibei, and Tai'an increased significantly between 16:00 and 17:00, however, the specific reasons remain to be further investigated. In general, NO_2 concentrations were higher and secondary HCHO concentrations were lower in the early morning, with the enhancement of photochemical reactions (08:00–13:00), NO_2 concentrations decreased rapidly and secondary HCHO concentrations increased gradually.

10
15
20
25

The significant diurnal variation in O_3 precursors contributes to the transition of O_3 formation sensitivity, as indicated by the FNR_{sec} , demonstrating a distinct single-peak pattern. As shown in Fig. 8 (j–l), FNR_{sec} increases sharply from 08:00 to 13:00, corresponding with considerable increases in O_3 VMRs. In cities like Hefei, Huaibei, and Tai'an, O_3 formation sensitivity starts in the VOC-limited regime (below the shaded area) at 08:00–09:00, gradually transitioning to the transition regime by 10:00–11:00. By 12:00–14:00, O_3 formation in Huaibei predominantly enters the NO_x -limited regime before shifting back to the transition regime after 15:00. Similarly, in Hefei and Tai'an, the NO_x -limited regime prevails from 12:00 to 16:00, shifting towards the transition regime after 17:00. Overall, O_3 formation sensitivity is VOC-limited or transition-regime dominant during periods of rapid O_3 concentration increases (08:00–12:00), shifting to transition or NO_x -limited

30

regimes when O₃ concentrations peak (12:00–14:00). We further investigated the diurnal characteristics of FNR_{sec} on O₃ exceedance days (MDA8 O₃ > 160 μg/m³). Compared to the entire observation period, FNR_{sec} on O₃ exceedance days exhibits a faster transition from 08:00 to 13:00 and prolonged persistence in the NO_x-limited regime.

5 The diurnal variation in the O₃ VMRs was very similar to that of FNR_{sec}, particularly from 08:00 to 13:00, both of which increased sharply. The exponential function was applied to fit the relationship between the O₃ concentration and FNR_{sec} values from 08:00 to 13:00 in Hefei, Huaibei, and Tai' an (Fig.9), and all three cities showed significant positive correlations, with Pearson correlation coefficients of 0.53 (P<0.01), 0.40 (P<0.01), and 0.52 (P<0.01) in Hefei, Huaibei, and Tai' an, respectively. Moreover, the exponential fitting is better on the O₃ exceedance days, and the correlation coefficients are higher, 0.69 (P<0.01), 0.59 (P<0.01), and 0.61 (P<0.01) in Hefei, Huaibei, and Tai' an, respectively. This indicates that the dependence of the O₃ production rate on its precursors rapidly shifts with increasing O₃ concentration, particularly on O₃ exceedance days. These changes also suggest that the dependence of O₃ on its precursors is extremely complex, and the precise control of O₃ pollution requires the identification of O₃ formation sensitivity mechanisms with high temporal resolution and targeted control of O₃ precursor concentrations.

15 Owing to the limitations of the observational data, the analysis of diurnal transitions in surface O₃ formation sensitivity is limited to three cities in eastern China. Here, other cities in eastern China were further investigated using satellite observations, and we construct conventional FNR using TROPOMI observed NO₂ and HCHO VCD from May to September 2018–2022. In order to avoid the misjudgment of O₃ formation sensitivity caused by arbitrary selection of FNR thresholds, A third-order polynomial model was applied to investigate the empirical relationship between TROPOMI FNR and surface O₃ VMRs, which has been widely used in other studies (Ren et al., 2022b). Since the TROPOMI observed surface O₃ VMRs can be obtained after November 2021 in China, we only collected the relationship between TROPOMI FNR and surface O₃ VMRs from May to September, 2022. The third-order polynomial fitting relationship between surface O₃ VMRs and TROPOMI FNR is shown in Fig. 10a, assuming that the peak of the curve (with a slope of 0) marks the transition from the VOC-limited regime to the NO_x-limited regime, the transition regime is defined as a range of slopes between -3 and +3 (Ren et al., 2022b). Through the third-order polynomial model, the TROPOMI FNR threshold in eastern China was determined, which are FNR <2.1 for VOC-limited regime, FNR>3.2 for NO_x-limited regime.

25 Figure 11 shows the occurrence probabilities of the VOC-limited regime, transition limited regime, and NO_x-limited regime spatial distributions derived from TROPOMI observations in eastern China during May–September, 2018–2022. Since the TROPOMI satellite usually transits around 13:30, it can represent the spatial distribution of midday O₃ formation sensitivity in eastern China. Apparently, the midday O₃ formation sensitivity of most cities in eastern China is under NO_x-limited regime, only several cities in the northern part of the NCP and Yangtze River Delta are mainly controlled by VOC-limited regime. In addition, Fig. 10b–d shows the trend of the area proportion of VOC-limited regime, transition regime, and NO_x-limited regime in the eastern China, in which the area proportion of VOC-limited regime and transition regime decreases at a rate of 0.62% and 0.18% per year, respectively. While the NO_x-limited regime area proportion increased at a rate of 0.80% per year. More importantly, although there is a significant monthly variation in the area proportion of O₃ formation sensitivity, it is usually

below 50% in May and September, and below 25% in June–August, that is, NO_x-limited regime dominates the midday O₃ formation sensitivity in eastern China. Due to China's strict control of NO_x emissions in recent years, the surface O₃ formation sensitivity in many areas of China has shown a transition from the VOC-limited regime to the transition regime or NO_x-limited regime.

5 In conclusion, significant diurnal transitions in surface O₃ formation sensitivity primarily stem from fluctuations in O₃ precursors. Early morning conditions (08:00–09:00) are mainly VOC-limited regime, shifting to a NO_x-limited regime by midday (12:00–14:00). In addition, the area proportion of VOC-limited regime was also declining, while the NO_x-limited regime area proportion was increasing. Consequently, the substantial reduction in NO_x emissions across eastern China has led to pronounced opposite trends in the low (increased) and peak (decreased) surface O₃ concentrations, and the surface O₃ formation sensitivity to VOCs is generally weakened year by year. Accordingly, the O₃ improvement benefits of VOCs emission reduction may become weaker, while the O₃ improvement benefits of NO_x emission reduction become larger. Furthermore, the long-distance transport of VOCs has a diminished impact on O₃ concentrations due to chemical losses from OH radical oxidation during transport, highlighting NO_x emission reductions as pivotal for intercity and even long-distance efforts to mitigate regional O₃ pollution (Wang et al., 2023b).

15 4 Discussions

Previous analyses have shown that the trend of low O₃ concentrations in eastern China is increasing, whereas the trend of peak O₃ concentrations is decreasing. The opposite trend is mainly driven by anthropogenic emissions. Significant NO_x emission reductions dominate the reduction in peak O₃ concentrations in eastern China, owing to the diurnal transition in surface O₃ formation sensitivity. The discussion focuses on the reasons for the differences in the O₃ trend statistics for 2017–2022 and 2017–2021, and the reasons for the possible increase in nighttime O₃.

As described in section 3.2, the trends for the monthly mean observed, meteorological, and anthropogenic 98th O₃ percentiles concentrations during May–September 2017–2021 are -0.363 ppb/year, -0.119 ppb/year (-33%), and -0.244 ppb/year (-67%), respectively (Table 1), and the trends for the monthly mean observed, meteorological, and anthropogenic 2nd O₃ percentiles concentrations are 0.027 ppb/year, -0.044 ppb/year (-163%), 0.071 ppb/year (263%), respectively. However, the trends of monthly mean observed, meteorological and anthropogenic of 98th O₃ percentiles during May–September 2017–2022 are -0.178 ppb/year, 0.005 ppb/year (3%) and -0.183 ppb/year (-103%), respectively, and the trends of the observed, meteorological and anthropogenic of 2nd O₃ percentiles during May–September 2017–2022 are 0.115 ppb/year, 0.008 ppb/year (7%) and 0.107 ppb/year (93%), respectively. Although anthropogenic emissions dominated variations in O₃ trends (May–September 2017–2022 and May–September 2017–2021), meteorological effects on O₃ trends cannot be ignored, particularly in 2022. Shadowed by mid-latitude atmospheric circulation, tropical sea–air coupling, and local land–air feedback processes, a record-breaking super-heatwave event occurred in most cities in eastern China in the summer of 2022, and some cities broke their highest temperature records (Zhang et al., 2023a; Zhang et al., 2022). The most important meteorological variables in the

MLR model were daily maximum temperature and RH (Tables S2 and S3). The temperature in eastern China showed that the monthly mean nighttime (daytime) temperature in June–August 2022 was 1.0 °C (1.1 °C), 0.8 °C (1.4 °C) and 2.2 °C (2.8 °C) higher than the monthly mean nighttime (daytime) temperature in June–August 2021, respectively (Fig. 12). The monthly mean nighttime (daytime) RH in eastern China in 2022 was 3.2% (3.1%), 1.9% (4.5%), and 9.4% (11%) lower than the monthly mean nighttime (daytime) RH in June–August 2021, respectively. Li et al. (2024) revealed that a sustained heatwave of extremely hot and dry summers in 2022 accelerate photochemical O₃ production by increasing anthropogenic and biogenic emissions and exacerbate O₃ accumulation by inhibiting dry deposition due to water-starved vegetation, resulting in an increase in O₃ pollution by more than 30% in urban areas. Our results also showed an increase in the meteorological components in the 98th and 2nd O₃ percentiles in 2022 relative to the meteorological components in the 98th and 2nd O₃ percentiles in 2021 (Fig.6). Therefore, extremely hot and dry weather in 2022 will increase the peak and low O₃ concentrations in eastern China, which is probably the main reason for the difference between the May and September 2017–2021 and May–September 2017–2022 meteorological component trends.

Overall, Meteorological conditions affected O₃ concentrations in three ways. The first is the effect on the photochemical reaction rates (Bloomer et al., 2009), which are affected by rising temperatures and increasing solar radiation intensity, leading to higher O₃ concentrations. Second, the effect on O₃ precursors, high temperature promotes an increase in VOCs emissions from land surface vegetation (Churkina et al., 2017), which further leads to an increase in the O₃ concentration. However, favorable meteorological conditions, such as high wind speed and precipitation, can reduce the O₃ precursor concentrations (Mousavinezhad et al., 2021), thereby reducing the O₃ concentration. Finally, transmission and regional transport also affect the distribution of O₃ in cities (Lang et al., 2021). However, the frequency of extreme weather events such as the super-heatwave event in 2022 is increasing (Jin et al., 2021; Zhang et al., 2015) in eastern China. In the context of the current warming climate, heat waves of extremely hot and dry conditions can elevate O₃ concentrations by increasing photochemical rates and promoting natural emissions (e.g., soil emissions of NO_x and vegetation emissions of VOCs), and meteorological components may have an increasing influence on O₃ trends.

Figure 6b shows that the observed increase in 2nd O₃ percentile was mainly concentrated after 2020, up to 0.44 ppb/year. The meteorological components did not change significantly in 2020 and 2021 but considerably increased in 2022, with a trend of 0.17 ppb/year 2020–2022. This rapid increase in 2nd O₃ percentile is mainly caused by anthropogenic emissions, with a trend of 0.27 ppb/year 2020–2022. Owing to the impact of the COVID–19 pandemic, the decrease in NO_x concentrations was most significant in 2020–2022 (Fig.2b), and the substantial reduction in NO_x concentrations weakened the O₃ titration of NO, resulting in an increase in nighttime O₃ concentrations, which was also confirmed by the significant negative correlation between the trend of the 98th NO₂ percentile and the trend of the 2nd O₃ percentiles during May–September 2017–2022 (Fig.5b). A recent study showed that nighttime O₃ depletion in China is mainly caused by the wet–scavenging effect and O₃ titration from fresh NO emissions (Li et al., 2023). The wet–scavenging effect was similar to the effect of precipitation, the higher the ambient humidity, the more conducive it was to O₃ depletion. The RH at night increased slowly in eastern China during May–September of 2017–2021 (Fig.12b), and the nighttime RH in 2020 and 2021 was higher than that in other years. Moreover, a

general wetting trend has been detected in eastern China during the summer in recent years (Hu et al., 2021), which is largely related to the increase in summer Precipitation and decrease in summer Potential Evapotranspiration. RH had the most significant effect on 2nd O₃ percentile trends according to MLR results (Table S2). Therefore, the meteorological component had an inhibitory effect on the increase in the 2nd O₃ percentile trends during May–September 2017–2021. However, owing to the significant emission reduction of NO_x concentrations, the titration of NO_x was weakened, and the decrease in O₃ depletion at night led to an increase in the overall 2nd O₃ percentile trends.

Owing to the limitations of the observational data, the analysis of surface O₃ precursors and O₃ formation sensitivity is limited to three cities in eastern China. Although other cities in eastern China were further investigated using satellite observations, TROPOMI only provides observation results for column concentrations at approximately 13:30 each day, which did not allow us to obtain diurnal variations in the O₃ formation sensitivity. Further observations must be extended to other cities to investigate the relationship between O₃ and its precursors more comprehensively.

In conclusion, owing to the impact of the COVID–19 pandemic (significant decrease in NO_x concentrations) and unfavorable meteorological conditions (high relative humidity) in 2020 and 2021 in eastern China, the 98th O₃ percentile concentration in 2020 and 2021 was lower (compared to the 98th O₃ percentile concentration in 2018 and 2019), while the 2nd O₃ percentile concentration showed a rapid upward trend. In addition, the extremely hot and dry meteorological conditions in 2022 will increase the 98th and 2nd O₃ percentile concentrations, weakening the decreasing trend in peak O₃ concentrations and increasing the upward trend at low O₃ concentrations.

5 Conclusions

In this study, we investigated urban–scale O₃ trends in densely populated areas of eastern China using multiple data sources. Through long–term records of surface O₃ and related parameters at 105 urban air quality monitoring sites in eastern China from May to September of 2017 to 2022, we found opposite trends for low and peak surface O₃ concentrations. Statistical results showed that low O₃ concentrations increased significantly (0.06 ppb/year, 0.3% per year), while peak O₃ concentrations decreased considerably (-0.39 ppb/year, -0.5% per year). Anthropogenic emissions were the main driver of both trends, although meteorological effects also played a role.

Based on long–term MAX–DOAS observations in Hefei, Huaibei, and Tai'an, we found that surface O₃ formation sensitivity in the early morning (8:00–9:00) was mainly controlled by VOC concentrations, shifting to an NO_x–limited regime by midday (12:00–14:00). Moreover, O₃ formation sensitivity is in the VOC–limited regime or transition regime during periods of sharp increases in O₃ concentrations (8:00–11:00) and usually in the transition or NO_x–limited regime when O₃ concentration peaks (11:00–14:00). Therefore, the decline in peak O₃ concentrations was attributed to the significant reduction in NO_x concentrations. To further suppress peak O₃ concentrations and reduce the number of O₃ exceedance days, controlling NO_x emissions should not be neglected. The increase in low O₃ concentrations can also be attributed to anthropogenic emissions and meteorological effects. Extremely hot and dry conditions can elevate O₃ concentrations by increasing

photochemical rates, promoting natural emissions, and depressing nighttime O₃ depletion by impairing the wet-scavenging effect. Additionally, a substantial reduction in NO_x concentrations weakened O₃ titration from fresh NO emissions and increased nighttime O₃ concentrations.

Our results highlight the positive impact of NO_x reduction in controlling peak O₃ levels. In response to the current severe O₃ pollution in China, it is crucial to consider the regular transitions in O₃ formation sensitivity throughout the day when formulating O₃ prevention and control policies. When O₃ concentrations are about to peak, strict control of NO_x emissions is necessary. This study provides novel insights into the spatiotemporal variability of O₃ formation sensitivity in eastern China and will be further expanded at different altitude levels in our future studies.

Author contributions. Cheng Liu, Chengzhi Xing, and Yujia, Chen conceived and supervised the study; Zhuang Wang analyzed the data; Zhuang Wang wrote the manuscript with input from Cheng Liu, Chengzhi Xing, and Yujia Chen; Chune Shi, and Hao Zhang reviewed and commented on the paper; All authors contributed to discuss the results and revised manuscript.

Competing interests. The authors declare that they have no competing interests.

Acknowledgments. Many thanks to Editor Jeffrey Geddes and the three reviewers for their time and expertise. We would like to express our gratitude to Fusheng Mou and SuWen Li of Huaibei Normal University for their assistance. We would like to thank the Ministry of Ecology and Environment of China for the O₃, NO₂ and CO data. We would like to thank the ERA5 data developers and TROPOMI data developers for providing free and open source materials.

Financial support. This research was supported by grants from the Anhui Provincial Natural Science Foundation "Jianghuai Meteorological" Joint Fund (2208085UQ04), National Natural Science Foundation of China (U21A2027, 42207113), Anhui Meteorological Bureau Special Programme for Innovation and Development (CXB202303), East China Regional Meteorological Science and Technology Collaborative Innovation Fund (QYHZ202317), and China Meteorological Administration " Application of quantum technology in meteorological detection " Youth Innovation Team Project (No.CMA2024QN11).

References

- Bao, J., Li, H., Wu, Z., Zhang, X., Zhang, H., Li, Y., Qian, J., Chen, J., and Deng, L.: Atmospheric carbonyls in a heavy ozone pollution episode at a metropolis in Southwest China: Characteristics, health risk assessment, sources analysis, *J. Environ. Sci-China*, 113, 40-54, 10.1016/j.jes.2021.05.029, 2022.
- Bauwens, M., Verreyken, B., Stavrakou, T., Müller, J. F., and Smedt, I. D.: Spaceborne evidence for significant anthropogenic VOC trends in Asian cities over 2005–2019, *Environ. Res. Lett.*, 17, 10.1088/1748-9326/ac46eb, 2022.
- Bloomer, B. J., Stehr, J. W., Piety, C. A., Salawitch, R. J., and Dickerson, R. R.: Observed relationships of ozone air pollution with temperature and emissions, *Geophys. Res. Lett.*, 36, 10.1029/2009gl037308, 2009.
- Chan, K. L., Wang, S., Liu, C., Zhou, B., Wenig, M. O., and Saiz-Lopez, A.: On the summertime air quality and related photochemical processes in the megacity Shanghai, China, *Sci. Total Environ.*, 580, 974-983, 10.1016/j.scitotenv.2016.12.052, 2017.

- Churkina, G., Kuik, F., Bonn, B., Lauer, A., Grote, R., Tomiak, K., and Butler, T. M.: Effect of VOC Emissions from Vegetation on Air Quality in Berlin during a Heatwave, *Environ. Sci. Technol.*, 51, 6120-6130, 10.1021/acs.est.6b06514, 2017.
- Chinese State Council: Action Plan on Air Pollution Prevention and Control (in Chinese), available at: http://www.gov.cn/zwggk/2013-09/12/content_2486773.htm (last access: 1 January 2024), 2013
- 5 Chinese State Council: Three-Year Action Plan on Defending the Blue Sky (in Chinese), available at: http://www.gov.cn/zhengce/content/2018-07/03/content_5303158.htm (last access: 1 January 2024), 2018.
- Cooper, O. R., Gao, R. S., Tarasick, D., Leblanc, T., and Sweeney, C.: Long-term ozone trends at rural ozone monitoring sites across the United States, 1990–2010, *J. Geophys. Res.-atmos.*, 117, 10.1029/2012jd018261, 2012.
- 10 Cynthia Lin, C. Y., Jacob, D. J., Munger, J. W., and Fiore, A. M.: Increasing background ozone in surface air over the United States, *Geophys. Res. Lett.*, 27, 3465-3468, 2000.
- De Smedt, I., Theys, N., Yu, H., Danckaert, T., Lerot, C., Compernelle, S., Van Roozendael, M., Richter, A., Hilboll, A., Peters, E., Pedernana, M., Loyola, D., Beirle, S., Wagner, T., Eskes, H., van Geffen, J., Boersma, K. F., and Veeffkind, P.: Algorithm theoretical baseline for formaldehyde retrievals from S5P TROPOMI and from the QA4ECV project, *Atmos. Meas. Tech.*, 11, 2395-2426, 10.5194/amt-11-2395-2018, 2018.
- 15 De Smedt, I., Pinardi, G., Vigouroux, C., Compernelle, S., Bais, A., Benavent, N., Boersma, F., Chan, K.-L., Donner, S., Eichmann, K.-U., Hedelt, P., Hendrick, F., Irie, H., Kumar, V., Lambert, J.-C., Langerock, B., Lerot, C., Liu, C., Loyola, D., Peters, A., Richter, A., Rivera Cárdenas, C., Romahn, F., Ryan, R. G., Sinha, V., Theys, N., Vlietinck, J., Wagner, T., Wang, T., Yu, H., and Van Roozendael, M.: Comparative assessment of TROPOMI and OMI formaldehyde observations and validation against MAX-DOAS network column measurements, *Atmos. Chem. Phys.*, 21, 12561-12593, 10.5194/acp-21-12561-2021,
- 20 2021.
- Dimitropoulou, E., Hendrick, F., Pinardi, G., Friedrich, M. M., Merlaud, A., Tack, F., De Longueville, H., Fayt, C., Hermans, C., Laffineur, Q., Fierens, F., and Van Roozendael, M.: Validation of TROPOMI tropospheric NO₂ columns using dual-scan multi-axis differential optical absorption spectroscopy (MAX-DOAS) measurements in Uccle, Brussels, *Atmos. Meas. Tech.*, 13, 5165-5191, 10.5194/amt-13-5165-2020, 2020.
- 25 Ding, J., Dai, Q., Fan, W., Lu, M., Zhang, Y., Han, S., and Feng, Y.: Impacts of meteorology and precursor emission change on O₃ variation in Tianjin, China from 2015 to 2021, *J. Environ. Sci-China*, 126, 506-516, 10.1016/j.jes.2022.03.010, 2023.
- Gao, A., Wang, J., Poetzsch, J., Li, S., Gao, B., Wang, P., Luo, J., Fang, X., Li, J., Hu, J., Gao, J., and Zhang, H.: Coordinated health effects attributable to particulate matter and other pollutants exposures in the North China Plain, *Environ. Res.*, 208, 10.1016/j.envres.2021.112671, 2022.
- 30 Garcia, A. R., Volkamer, R., Molina, L. T., Molina, M. J., Samuelson, J., Mellqvist, J., Galle, B., Herndon, S. C., and Kolb, C. E.: Separation of emitted and photochemical formaldehyde in Mexico City using a statistical analysis and a new pair of gas-phase tracers, *Atmos. Chem. Phys.*, 12, 4545–4557, 2006.
- Gaudel, A., Cooper, O. R., Chang, K.-L., Bourgeois, I., Ziemke, J. R., Strode, S. A., Oman, L. D., Sellitto, P., Nédélec, P., and Blot, R.: Aircraft observations since the 1990s reveal increases of tropospheric ozone at multiple locations across the Northern Hemisphere, *Sci. Adv.*, 6, eaba8272, 2020.
- 35 Guan, Y., Xiao, Y., Rong, B., Zhang, N., and Chu, C.: Long-term health impacts attributable to PM_{2.5} and ozone pollution in China's most polluted region during 2015–2020, *J. Clean. Prod.*, 321, 10.1016/j.jclepro.2021.128970, 2021.
- Han, H., Liu, J., Shu, L., Wang, T., and Yuan, H.: Local and synoptic meteorological influences on daily variability in summertime surface ozone in eastern China, *Atmos. Chem. Phys.*, 20, 203-222, 10.5194/acp-20-203-2020, 2020.
- 40 Heue, K. P., Riede, H., Walter, D., Brenninkmeijer, C. A. M., Wagner, T., Frieß, U., Platt, U., Zahn, A., Stratmann, G., and Ziereis, H.: CARIBIC DOAS observations of nitrous acid and formaldehyde in a large convective cloud, *Atmos. Chem. Phys.*, 14, 6621-6642, 10.5194/acp-14-6621-2014, 2014.
- Hong, Q., Liu, C., Chan, K. L., Hu, Q., Xie, Z., Liu, H., Si, F., and Liu, J.: Ship-based MAX-DOAS measurements of

- tropospheric NO₂, SO₂, and HCHO distribution along the Yangtze River, *Atmos. Chem. Phys.*, 18, 5931-5951, 10.5194/acp-18-5931-2018, 2018.
- Hong, Q., Zhu, L., Xing, C., Hu, Q., Lin, H., Zhang, C., Zhao, C., Liu, T., Su, W., and Liu, C.: Inferring vertical variability and diurnal evolution of O₃ formation sensitivity based on the vertical distribution of summertime HCHO and NO₂ in Guangzhou, China, *Sci. Total Environ.*, 827, 10.1016/j.scitotenv.2022.154045, 2022.
- Hu, W., She, D., Xia, J., He, B., and Hu, C.: Dominant patterns of dryness/wetness variability in the Huang-Huai-Hai River Basin and its relationship with multiscale climate oscillations, *Atmos. Res.*, 247, 105148, 2021.
- Jacob, D. J., Logan, J. A., and Murti, P. P.: Effect of rising Asian emissions on surface ozone in the United States, *Geophys. Res. Lett.*, 26, 2175-2178, 1999.
- Jin, H., Chen, X., Zhong, R., and Duan, K.: Frequency analysis of extreme precipitation in different regions of the Huaihe River Basin, *Int. J. Climatol.*, 42, 3517-3536, 10.1002/joc.7430, 2021.
- Lang, J., Liang, X., Li, S., Zhou, Y., Chen, D., Zhang, Y., and Xu, L.: Understanding the impact of vehicular emissions on air pollution from the perspective of regional transport: A case study of the Beijing-Tianjin-Hebei region in China, *Sci. Total Environ.*, 785, 10.1016/j.scitotenv.2021.147304, 2021.
- Lefohn, A. S., Hazucha, M. J., Shadwick, D., and Adams, W. C.: An alternative form and level of the human health ozone standard, *Inhal. Toxicol.*, 22, 999-1011, 2010.
- Li, J., Lu, K., Lv, W., Li, J., Zhong, L., Ou, Y., Chen, D., Huang, X., and Zhang, Y.: Fast increasing of surface ozone concentrations in Pearl River Delta characterized by a regional air quality monitoring network during 2006–2011, *J. Environ. Sci-China*, 26, 23-36, 10.1016/s1001-0742(13)60377-0, 2014.
- Li, K., Jacob, D. J., Liao, H., Shen, L., Zhang, Q., and Bates, K. H.: Anthropogenic drivers of 2013–2017 trends in summer surface ozone in China, *Proc. Natl. Acad. Sci.*, 116, 422-427, 10.1073/pnas.1812168116, 2018.
- Li, K., Jacob, D. J., Shen, L., Lu, X., De Smedt, I., and Liao, H.: Increases in surface ozone pollution in China from 2013 to 2019: anthropogenic and meteorological influences, *Atmos. Chem. Phys.*, 20, 11423-11433, 10.5194/acp-20-11423-2020, 2020a.
- Li, K., Jacob, D. J., Liao, H., Qiu, Y., Shen, L., Zhai, S., Bates, K. H., Sulprizio, M. P., Song, S., Lu, X., Zhang, Q., Zheng, B., Zhang, Y., Zhang, J., Lee, H. C., and Kuk, S. K.: Ozone pollution in the North China Plain spreading into the late-winter haze season, *Proc. Natl. Acad. Sci.*, 118, 10.1073/pnas.2015797118, 2021.
- Li, L., Yang, W., Xie, S., and Wu, Y.: Estimations and uncertainty of biogenic volatile organic compound emission inventory in China for 2008–2018, *Sci. Total Environ.*, 733, 10.1016/j.scitotenv.2020.139301, 2020b.
- Li, M., Huang, X., Yan, D., Lai, S., Zhang, Z., Zhu, L., Lu, Y., Jiang, X., Wang, N., Wang, T., Song, Y., and Ding, A.: Coping with the concurrent heatwaves and ozone extremes in China under a warming climate, *Sci. Bull.*, 10.1016/j.scib.2024.05.034, 2024.
- Li, M., Liu, H., Geng, G., Hong, C., Liu, F., Song, Y., Tong, D., Zheng, B., Cui, H., Man, H., Zhang, Q., and He, K.: Anthropogenic emission inventories in China: a review, *Natl. Sci. Rev.*, 4, 834-866, 10.1093/nsr/nwx150, 2017.
- Li, X.-B., Yuan, B., Parrish, D. D., Chen, D., Song, Y., Yang, S., Liu, Z., and Shao, M.: Long-term trend of ozone in southern China reveals future mitigation strategy for air pollution, *Atmos. Environ.*, 269, 10.1016/j.atmosenv.2021.118869, 2022.
- Li, X., Ren, J., Huang, R., Chen, L., Li, Y., Qiao, X., Cheng, Y., Zhao, B., Yin, D., Gao, D., Sun, Y., and Zhang, F.: The Aggravation of Summertime Nocturnal Ozone Pollution in China and Its Potential Impact on the Trend of Nitrate Aerosols, *Geophys. Res. Lett.*, 50, 10.1029/2023gl103242, 2023.
- Lin, H., Xing, C., Hong, Q., Liu, C., Ji, X., Liu, T., Lin, J., Lu, C., Tan, W., Li, Q., and Liu, H.: Diagnosis of Ozone Formation Sensitivities in Different Height Layers via MAX-DOAS Observations in Guangzhou, *J. Geophys. Res-atmos.*, 127, 10.1029/2022jd036803, 2022.

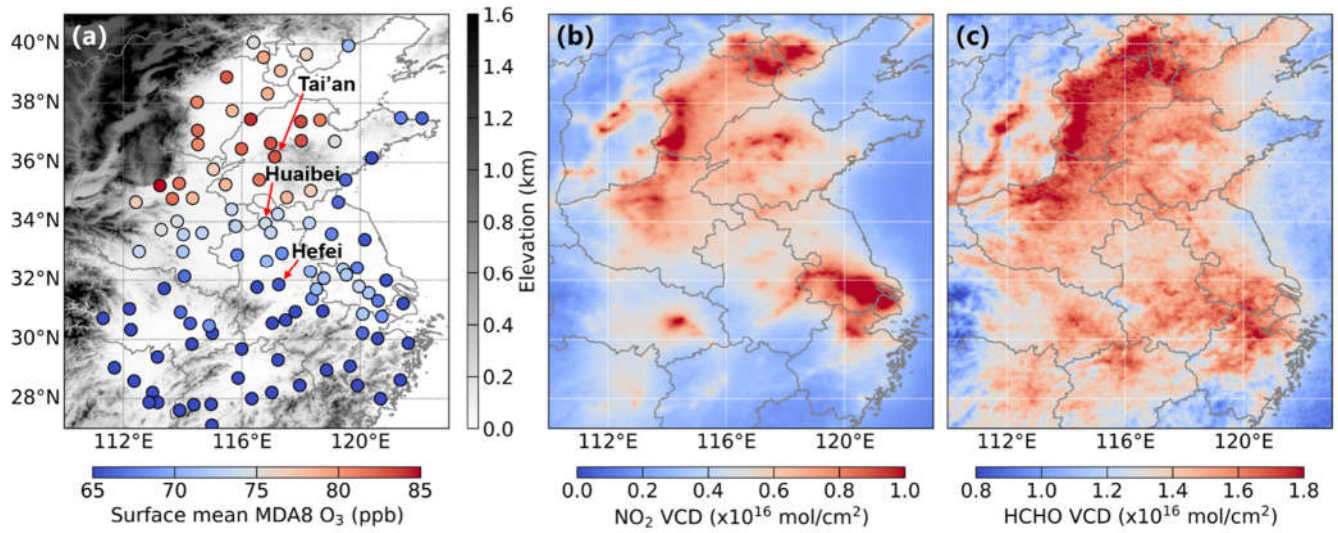
- Lin, N., Wang, Y., Zhang, Y., and Yang, K.: A large decline of tropospheric NO₂ in China observed from space by SNPP OMPS, *Sci. Total Environ.*, 675, 337-342, 10.1016/j.scitotenv.2019.04.090, 2019.
- 5 Liu, C., Hu, Q., Zhang, C., Xia, C., Yin, H., Su, W., Wang, X., Xu, Y., and Zhang, Z.: First Chinese ultraviolet–visible hyperspectral satellite instrument implicating global air quality during the COVID-19 pandemic in early 2020, *Light Sci. Appl.*, 11, 10.1038/s41377-022-00722-x, 2022a.
- Liu, C., Xing, C., Hu, Q., Li, Q., Liu, H., Hong, Q., Tan, W., Ji, X., Lin, H., Lu, C., Lin, J., Liu, H., Wei, S., Chen, J., Yang, K., Wang, S., Liu, T., and Chen, Y.: Ground-Based Hyperspectral Stereoscopic Remote Sensing Network: A Promising Strategy to Learn Coordinated Control of O₃ and PM_{2.5} over China, *Engineering*, 19, 71-83, 10.1016/j.eng.2021.02.019, 2022b.
- 10 Liu, J., Wang, S., Zhang, Y., Yan, Y., Zhu, J., Zhang, S., Wang, T., Tan, Y., and Zhou, B.: Investigation of formaldehyde sources and its relative emission intensity in shipping channel environment, *J. Environ. Sci-China*, 142, 142-154, 10.1016/j.jes.2023.06.020, 2024.
- Liu, Y., Geng, G., Cheng, J., Liu, Y., Xiao, Q., Liu, L., Shi, Q., Tong, D., He, K., and Zhang, Q.: Drivers of Increasing Ozone during the Two Phases of Clean Air Actions in China 2013–2020, *Environ. Sci. Technol.*, 57, 8954-8964, 10.1021/acs.est.3c00054, 2023.
- 15 Lu, C., Li, Q., Xing, C., Hu, Q., Tan, W., Lin, J., Zhang, Z., Tang, Z., Cheng, J., Chen, A., and Liu, C.: Identification of O₃ Sensitivity to Secondary HCHO and NO₂ Measured by MAX-DOAS in Four Cities in China, *Remote Sens.*, 16, 10.3390/rs16040662, 2024.
- Lu, X., Zhang, L., Wang, X., Gao, M., Li, K., Zhang, Y., Yue, X., and Zhang, Y.: Rapid Increases in Warm-Season Surface Ozone and Resulting Health Impact in China Since 2013, *Environ. Sci. Technol. Lett.*, 7, 240-247, 10.1021/acs.estlett.0c00171, 2020.
- 20 Ma, Y., Diao, Y., Zhang, B., Wang, W., Ren, X., Yang, D., Wang, M., Shi, X., and Zheng, J.: Detection of formaldehyde emissions from an industrial zone in the Yangtze River Delta region of China using a proton transfer reaction ion-drift chemical ionization mass spectrometer, *Atmos. Meas. Tech.*, 9, 6101-6116, 10.5194/amt-9-6101-2016, 2016.
- Ma, Z., Liu, C., Zhang, C., Liu, P., Ye, C., Xue, C., Zhao, D., Sun, J., Du, Y., Chai, F., and Mu, Y.: The levels, sources and reactivity of volatile organic compounds in a typical urban area of Northeast China, *J. Environ. Sci-China*, 79, 121-134, 10.1016/j.jes.2018.11.015, 2019.
- MacDonald, S. M., Oetjen, H., Mahajan, A. S., Whalley, L. K., Edwards, P. M., Heard, D. E., Jones, C. E., and Plane, J. M. C.: DOAS measurements of formaldehyde and glyoxal above a south-east Asian tropical rainforest, *Atmos. Chem. Phys.*, 12, 5949-5962, 10.5194/acp-12-5949-2012, 2012.
- 30 Mousavinezhad, S., Choi, Y., Pouyaei, A., Ghahremanloo, M., and Nelson, D. L.: A comprehensive investigation of surface ozone pollution in China, 2015–2019: Separating the contributions from meteorology and precursor emissions, *Atmos. Res.*, 257, 10.1016/j.atmosres.2021.105599, 2021.
- Possanzini, M., Di Palo, V., and Cecinato, A.: Sources and photodecomposition of formaldehyde and acetaldehyde in Rome ambient air, *Atmos. Environ.*, 36, 3195-3201, 2002.
- 35 Ren, B., Xie, P., Xu, J., Li, A., Qin, M., Hu, R., Zhang, T., Fan, G., Tian, X., Zhu, W., Hu, Z., Huang, Y., Li, X., Meng, F., Zhang, G., Tong, J., Ren, H., Zheng, J., Zhang, Z., and Lv, Y.: Vertical characteristics of NO₂ and HCHO, and the ozone formation regimes in Hefei, China, *Sci. Total Environ.*, 823, 10.1016/j.scitotenv.2022.153425, 2022a.
- Ren, J., Guo, F., and Xie, S.: Diagnosing ozone–NO_x–VOC sensitivity and revealing causes of ozone increases in China based on 2013–2021 satellite retrievals, *Atmos. Chem. Phys.*, 22, 15035-15047, 10.5194/acp-22-15035-2022, 2022b.
- 40 Song, Y., Xing, C., Liu, C., Lin, J., Wu, H., Liu, T., Lin, H., Zhang, C., Tan, W., Ji, X., Liu, H., and Li, Q.: Evaluation of transport processes over North China Plain and Yangtze River Delta using MAX-DOAS observations, *Atmos. Chem. Phys.*, 23, 1803-1824, 10.5194/acp-23-1803-2023, 2023.
- Su, W., Liu, C., Hu, Q., Fan, G., Xie, Z., Huang, X., Zhang, T., Chen, Z., Dong, Y., Ji, X., Liu, H., Wang, Z., and Liu, J.:

- Characterization of ozone in the lower troposphere during the 2016 G20 conference in Hangzhou, *Sci. Rep.*, 7, 10.1038/s41598-017-17646-x, 2017.
- Sun, X., Zhao, T., Bai, Y., Kong, S., Zheng, H., Hu, W., Ma, X., and Xiong, J.: Meteorology impact on PM_{2.5} change over a receptor region in the regional transport of air pollutants: observational study of recent emission reductions in central China, *Atmos. Chem. Phys.*, 22, 3579–3593, <https://doi.org/10.5194/acp-22-3579-2022>, 2022.
- Sun, Y., Yin, H., Liu, C., Zhang, L., Cheng, Y., Palm, M., Notholt, J., Lu, X., Vigouroux, C., Zheng, B., Wang, W., Jones, N., Shan, C., Qin, M., Tian, Y., Hu, Q., Meng, F., and Liu, J.: Mapping the drivers of formaldehyde (HCHO) variability from 2015 to 2019 over eastern China: insights from Fourier transform infrared observation and GEOS-Chem model simulation, *Atmos. Chem. Phys.*, 21, 6365-6387, 10.5194/acp-21-6365-2021, 2021.
- Taguchi, S., Hagiwara, M., Shibata, A., Fujinari, H., Matsumoto, S., Kuwata, M., Sazawa, K., Hata, N., and Kuramitz, H.: Investigation and modeling of diurnal variation in suburban ambient formaldehyde concentration, *Environ. Sci. Pollut. Res.*, 28, 13425-13438, 10.1007/s11356-020-11465-w, 2020.
- van Geffen, J., Boersma, K. F., Eskes, H., Sneep, M., ter Linden, M., Zara, M., and Veefkind, J. P.: S5P TROPOMI NO₂ slant column retrieval: method, stability, uncertainties and comparisons with OMI, *Atmos. Meas. Tech.*, 13, 1315-1335, 10.5194/amt-13-1315-2020, 2020.
- Veefkind, J. P., Aben, I., McMullan, K., Förster, H., de Vries, J., Otter, G., Claas, J., Eskes, H. J., de Haan, J. F., Kleipool, Q., van Weele, M., Hasekamp, O., Hoogeveen, R., Landgraf, J., Snel, R., Tol, P., Ingmann, P., Voors, R., Kruizinga, B., Vink, R., Visser, H., and Levelt, P. F.: TROPOMI on the ESA Sentinel-5 Precursor: A GMES mission for global observations of the atmospheric composition for climate, air quality and ozone layer applications, *Remote Sens. Environ.*, 120, 70-83, 10.1016/j.rse.2011.09.027, 2012.
- Wang, M., Chen, W., Shao, M., Lu, S., Zeng, L., and Hu, M.: Investigation of carbonyl compound sources at a rural site in the Yangtze River Delta region of China, *J. Environ. Sci-China*, 28, 128-136, 10.1016/j.jes.2014.12.001, 2015.
- Wang, N., Lyu, X., Deng, X., Huang, X., Jiang, F., and Ding, A.: Aggravating O₃ pollution due to NO_x emission control in eastern China, *Sci. Total Environ.*, 677, 732-744, 10.1016/j.scitotenv.2019.04.388, 2019.
- Wang, W., Parrish, D. D., Wang, S., Bao, F., Ni, R., Li, X., Yang, S., Wang, H., Cheng, Y., and Su, H.: Long-term trend of ozone pollution in China during 2014–2020: distinct seasonal and spatial characteristics and ozone sensitivity, *Atmos. Chem. Phys.*, 22, 8935-8949, 10.5194/acp-22-8935-2022, 2022a.
- Wang, Y., Yang, X., Wu, K., Mei, H., De Smedt, I., Wang, S., Fan, J., Lyu, S., and He, C.: Long-term trends of ozone and precursors from 2013 to 2020 in a megacity (Chengdu), China: Evidence of changing emissions and chemistry, *Atmos. Res.*, 278, 10.1016/j.atmosres.2022.106309, 2022b.
- Wang, Y., Zhao, Y., Liu, Y., Jiang, Y., Zheng, B., Xing, J., Liu, Y., Wang, S., and Nielsen, C. P.: Sustained emission reductions have restrained the ozone pollution over China, *Nat. Geosci.*, 16, 967-974, 10.1038/s41561-023-01284-2, 2023a.
- Wang, Y., Jiang, S., Huang, L., Lu, G., Kasemsan, M., Yaluk, E. A., Liu, H., Liao, J., Bian, J., Zhang, K., Chen, H., and Li, L.: Differences between VOCs and NO_x transport contributions, their impacts on O₃, and implications for O₃ pollution mitigation based on CMAQ simulation over the Yangtze River Delta, China, *Sci. Total Environ.*, 872, 10.1016/j.scitotenv.2023.162118, 2023b.
- Wang, Z., Shi, C., Zhang, H., Chen, Y., Chi, X., Xia, C., Wang, S., Zhu, Y., Zhang, K., Chen, X., Xing, C., and Liu, C.: Measurement report: Dust and anthropogenic aerosols' vertical distributions over northern China dense aerosols gathered at the top of the mixing layer, *Atmos. Chem. Phys.*, 23, 14271-14292, 10.5194/acp-23-14271-2023, 2023c.
- Wang, Z., Liu, C., Xie, Z., Hu, Q., Andreae, M. O., Dong, Y., Zhao, C., Liu, T., Zhu, Y., Liu, H., Xing, C., Tan, W., Ji, X., Lin, J., and Liu, J.: Elevated dust layers inhibit dissipation of heavy anthropogenic surface air pollution, *Atmos. Chem. Phys.*, 20, 14917-14932, 10.5194/acp-20-14917-2020, 2020.
- Weng, X., Forster, G. L., and Nowack, P.: A machine learning approach to quantify meteorological drivers of ozone pollution

- in China from 2015 to 2019, *Atmos. Chem. Phys.*, 22, 8385-8402, 10.5194/acp-22-8385-2022, 2022.
- Wood, E. C., Canagaratna, M. R., Herndon, S. C., Onasch, T. B., Kolb, C. E., Worsnop, D. R., Kroll, J. H., Knighton, W. B., Seila, R., Zavala, M., Molina, L. T., DeCarlo, P. F., Jimenez, J. L., Weinheimer, A. J., Knapp, D. J., Jobson, B. T., Stutz, J., Kuster, W. C., and Williams, E. J.: Investigation of the correlation between odd oxygen and secondary organic aerosol in Mexico City and Houston, *Atmos. Chem. Phys.*, 10, 8947-8968, 10.5194/acp-10-8947-2010, 2010.
- 5 Wu, Y., Chen, W., You, Y., Xie, Q., Jia, S., and Wang, X.: Quantitative impacts of vertical transport on the long-term trend of nocturnal ozone increase over the Pearl River Delta region during 2006–2019, *Atmos. Chem. Phys.*, 23, 453-469, 10.5194/acp-23-453-2023, 2023.
- Xing, C., Liu, C., Lin, J., Tan, W., and Liu, T.: VOCs hyperspectral imaging: A new insight into evaluate emissions and the corresponding health risk from industries, *J. Hazard. Mater.*, 461, 10.1016/j.jhazmat.2023.132573, 2024.
- 10 Xing, C., Liu, C., Hong, Q., Liu, H., Wu, H., Lin, J., Song, Y., Chen, Y., Liu, T., Hu, Q., Tan, W., and Lin, H.: Vertical distributions and potential sources of wintertime atmospheric pollutants and the corresponding ozone production on the coast of Bohai Sea, *J. Environ. Manage.*, 319, 10.1016/j.jenvman.2022.115721, 2022.
- Xue, J., Zhao, T., Luo, Y., Miao, C., Su, P., Liu, F., Zhang, G., Qin, S., Song, Y., Bu, N., and Xing, C.: Identification of ozone sensitivity for NO₂ and secondary HCHO based on MAX-DOAS measurements in northeast China, *Environ. Int.*, 160, 10.1016/j.envint.2021.107048, 2022.
- 15 Zhai, S., Jacob, D. J., Wang, X., Shen, L., Li, K., Zhang, Y., Gui, K., Zhao, T., and Liao, H.: Fine particulate matter (PM_{2.5}) trends in China, 2013–2018: separating contributions from anthropogenic emissions and meteorology, *Atmos. Chem. Phys.*, 19, 11031-11041, 10.5194/acp-19-11031-2019, 2019.
- 20 Zhang, Q., Zheng, Y., Tong, D., Shao, M., Wang, S., Zhang, Y., Xu, X., Wang, J., He, H., Liu, W., Ding, Y., Lei, Y., Li, J., Wang, Z., Zhang, X., Wang, Y., Cheng, J., Liu, Y., Shi, Q., Yan, L., Geng, G., Hong, C., Li, M., Liu, F., Zheng, B., Cao, J., Ding, A., Gao, J., Fu, Q., Huo, J., Liu, B., Liu, Z., Yang, F., He, K., and Hao, J.: Drivers of improved PM_{2.5} air quality in China from 2013 to 2017, *Proc. Natl. Acad. Sci.*, 116, 24463-24469, 10.1073/pnas.1907956116, 2019.
- Zhang, T., Deng, Y., Chen, J., Yang, S., and Dai, Y.: An energetics tale of the 2022 mega-heatwave over central-eastern China, *Npj Clim. Atmos. Sci.*, 6, 10.1038/s41612-023-00490-4, 2023a.
- 25 Zhang, T., Tam, C.-Y., Lau, N.-C., Wang, J., Yang, S., Chen, J., Yu, W., Jiang, X., and Gao, P.: Influences of the boreal winter Arctic Oscillation on the peak-summer compound heat waves over the Yangtze–Huaihe River basin: the North Atlantic capacitor effect, *Clim. Dyn.*, 59, 2331-2343, 10.1007/s00382-022-06212-5, 2022.
- Zhang, W., Pan, S., Cao, L., Cai, X., Zhang, K., Xu, Y., and Xu, W.: Changes in extreme climate events in eastern China during 1960–2013: A case study of the Huaihe River Basin, *Quat. Int.*, 380-381, 22-34, 10.1016/j.quaint.2014.12.038, 2015.
- 30 Zhang, X., Xu, W., Zhang, G., Lin, W., Zhao, H., Ren, S., Zhou, G., Chen, J., and Xu, X.: First long-term surface ozone variations at an agricultural site in the North China Plain: Evolution under changing meteorology and emissions, *Sci. Total Environ.*, 860, 10.1016/j.scitotenv.2022.160520, 2023b.
- Zhang, Y.-L. and Cao, F.: Fine particulate matter (PM_{2.5}) in China at a city level, *Sci. Rep.*, 5, 10.1038/srep14884, 2015.
- 35 Zheng, B., Tong, D., Li, M., Liu, F., Hong, C., Geng, G., Li, H., Li, X., Peng, L., Qi, J., Yan, L., Zhang, Y., Zhao, H., Zheng, Y., He, K., and Zhang, Q.: Trends in China's anthropogenic emissions since 2010 as the consequence of clean air actions, *Atmos. Chem. Phys.*, 18, 14095-14111, 10.5194/acp-18-14095-2018, 2018.

40

Figures:



5 **Fig.1.** Spatial distributions of O₃ and its precursors in eastern China. (a) Spatial distributions of surface mean MDA8 O₃ concentrations during May–September 2017–2022. The red arrow indicates the name of each city, which are equipped with ground-based MAX-DOAS observations. Spatial distributions of tropospheric mean (b) NO₂ and (c) HCHO VCD during May–September 2018–2022.

10

15

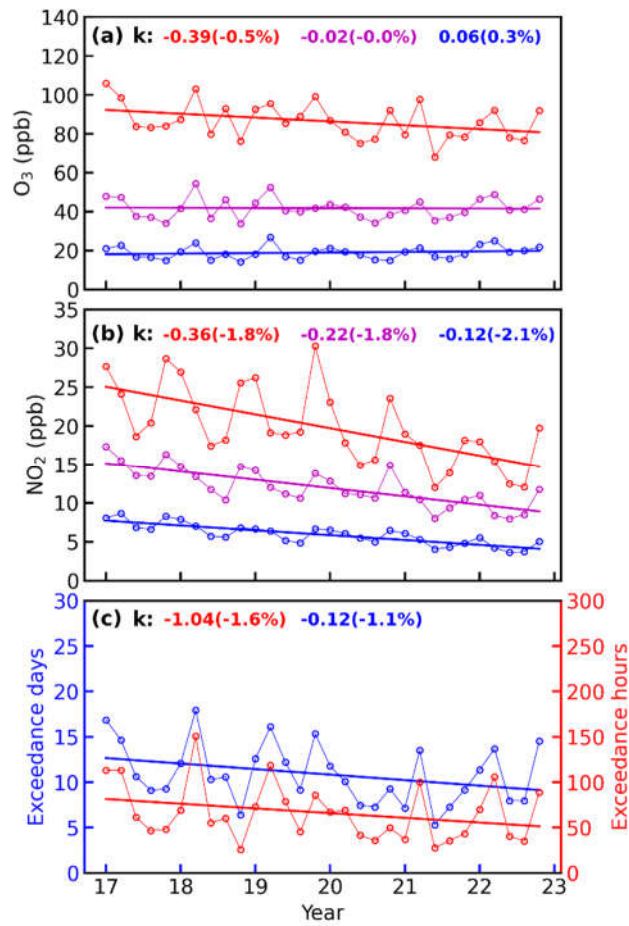


Fig.2. Trends of surface (a) O₃, (b) NO₂, (c) O₃ exceedance days and O₃ exceedance hours in eastern China during May–September 2017–2022. The red, magenta, and blue solid lines in (a) and (b) indicate the trends for the 98th, 50th, and 2nd percentiles, respectively. The labels on (a) and (b) represent the trends in O₃ and NO₂ for May–September 2017–2022, units: ppb/year. The labels on (c) represent the trends in O₃ exceedance days and O₃ exceedance hours for May–September 2017–2022. The percentage change is indicated in brackets.

5

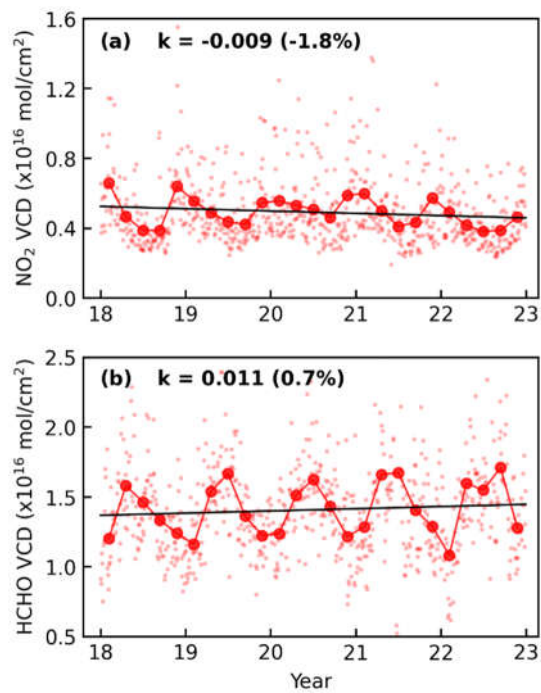


Fig.3. Trends of TROPOMI observed (a) NO₂ VCD, and (b) HCHO VCD averaged over eastern China during May–September 2018–2022. The labels at the top of each panel represent the trends in NO₂ VCD, and HCHO VCD, respectively. The percentage change is indicated in brackets. The light red dots in (a,b) represent the daily values, and the solid red dots are monthly mean values.

5

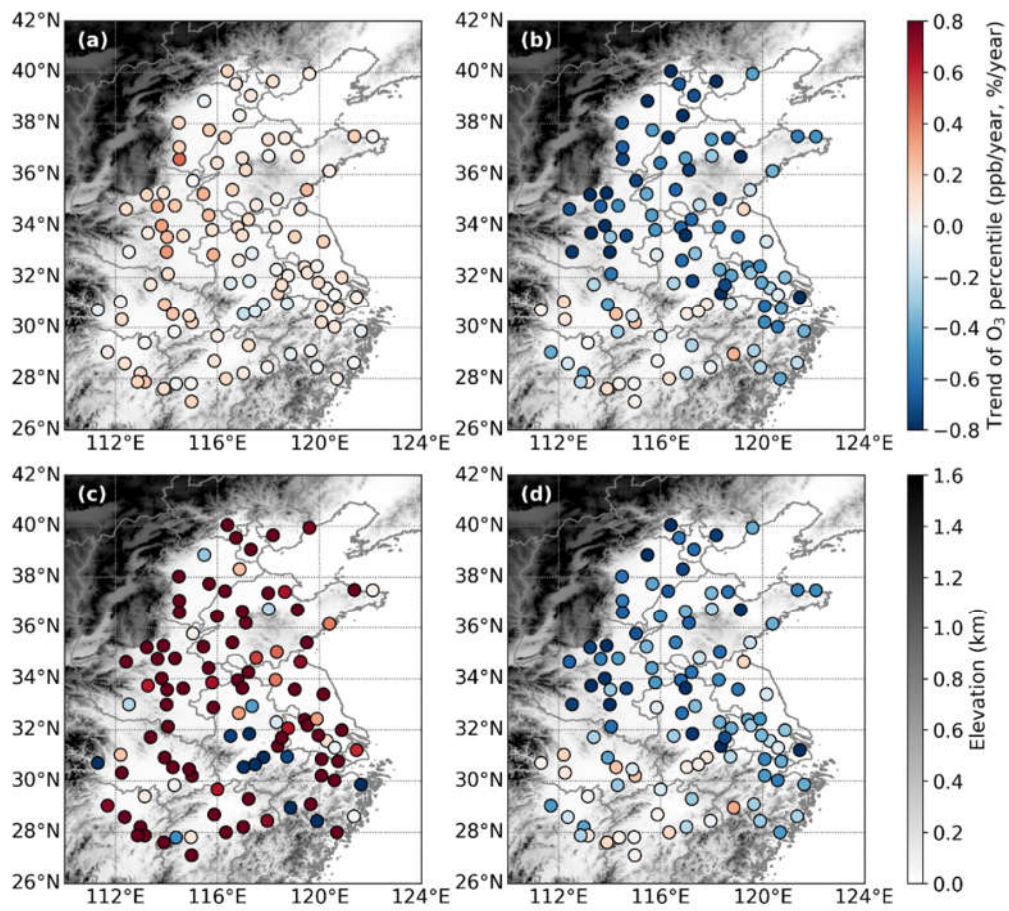


Fig.4. Trends of peak and low O₃ concentrations in eastern China. Trend of (a) 2% and (b) 98% O₃ percentiles, units: ppb/year, percentage variations in (c) 2% and (d) 98% O₃ percentile, units: %/year.

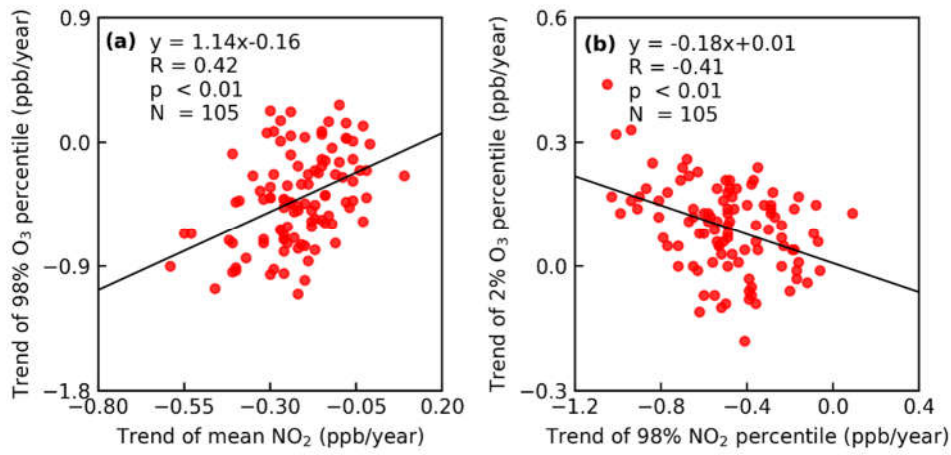


Fig.5. Scatterplots showing the relationships between the (a) trend of mean NO₂ concentrations and the trend of 98th O₃ percentiles, (b) trend of 98th NO₂ percentiles and trend of 2nd O₃ percentiles in each city of eastern China during May–September 2017–2022. The correlation coefficients are shown in the top left of each panel, N=number of cities.

5

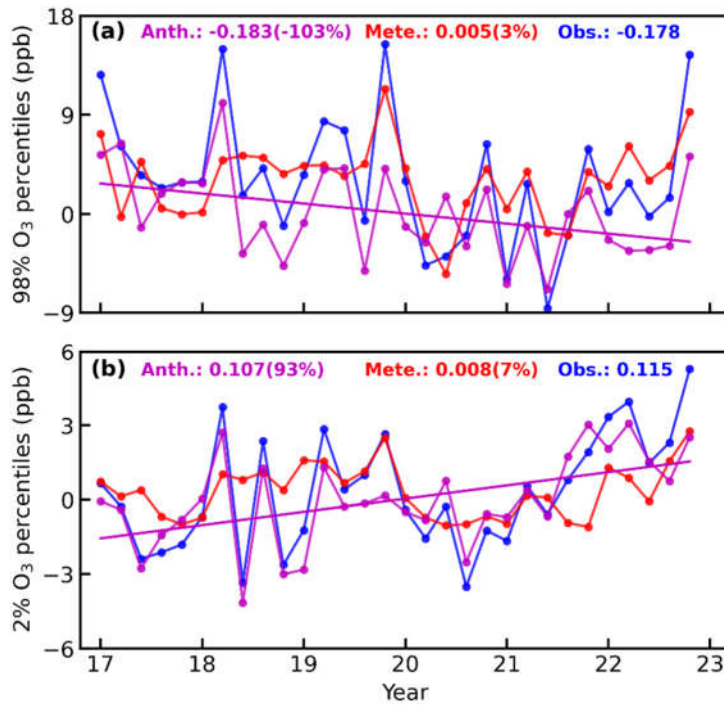
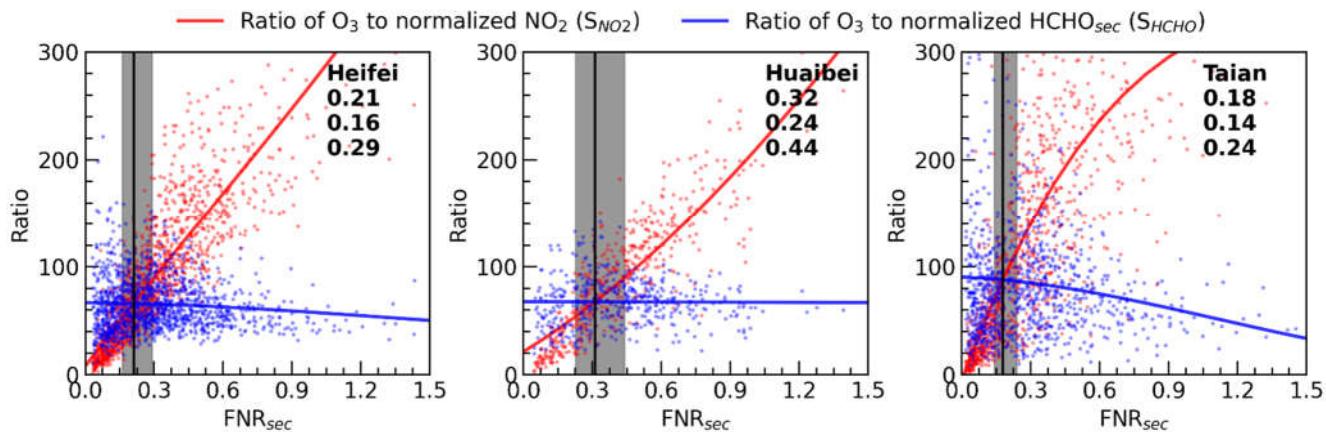


Fig.6. Trends of observed (blue lines), meteorological (red lines), and anthropogenic (magenta lines) (a) 98th and (b) 2nd O₃ percentiles component in eastern China during May–September 2017–2022. The labels at the top of each panel represent the trend in observed, meteorological, and anthropogenic components.



5 **Fig.7.** Three-order fitting of ratios of O₃ VMRs versus normalized NO₂ VMRs and ratios of O₃ VMRs versus normalized secondary HCHO VMRs in different FNR_{sec} values in Hefei, Huaibei, and Tai'an during May–September based on MAX–DOAS observations. The intersect at FNR_{sec} indicated by the black solid line. The vertical shadow indicates the relative difference between the ratios of O₃ VMRs versus normalized NO₂ VMRs and ratios of O₃ VMRs versus secondary HCHO VMRs within 25% (transition regime). The labels at the top right of each panel represent the intersect FNR_{sec} values and the thresholds for the NO_x-limited regime (high) and VOC-limited regime (low) in Hefei, Huaibei, and Tai'an, respectively.

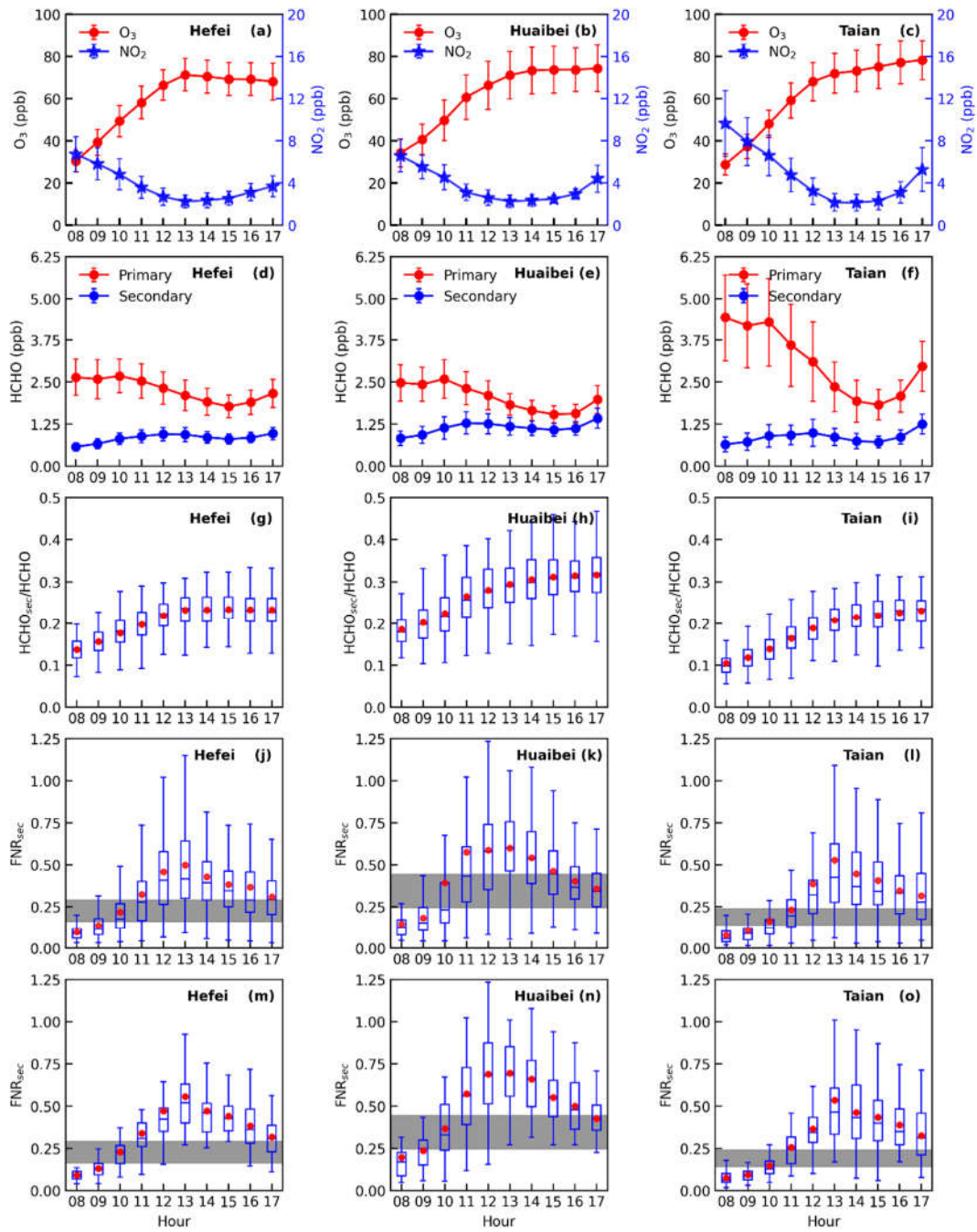


Fig.8. Diurnal variation of surface (a–c) O_3 and NO_2 VMRs, (d–f) HCHO VMRs contributed by primary and secondary sources, (g–i) the ratio of secondary HCHO to total HCHO VMRs, (j–l) FNR_{sec} during the whole observation, and (m–o) FNR_{sec} during O_3 exceedance day in Hefei, Huaibei, and Tai'an during May–September, respectively. The vertical bars in (a–f) represent the one standard deviation. The dot within the box indicates the mean value, the positions of box plots represent the 5th, 25th, 50th, 75th, 95th percentiles, respectively. The horizontal shadow in (j–o) represents the transition regime, the top of the shadow represents the NO_x -limited regime, and the bottom of the shadow represents the VOC-limited regime.

5

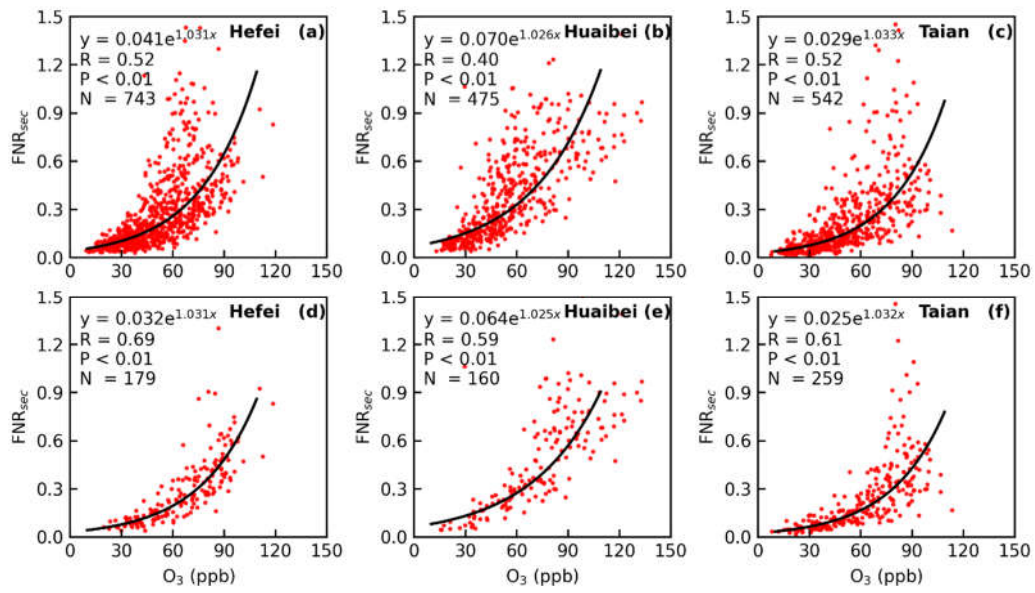


Fig.9. The relationship between the O₃ VMRs and FNR_{sec} during (a–c) the whole observation, and (d–f) the O₃ exceedance day from 08:00 to 13:00 in Hefei, Huaibei, and Tai'an, respectively. The black line represents the exponential fitting ($f(x) = A \times e^{B \times x}$). The fitting functions and correlation coefficients for exponential fit are shown at the top left of each panel, N=number of samples.

5

10

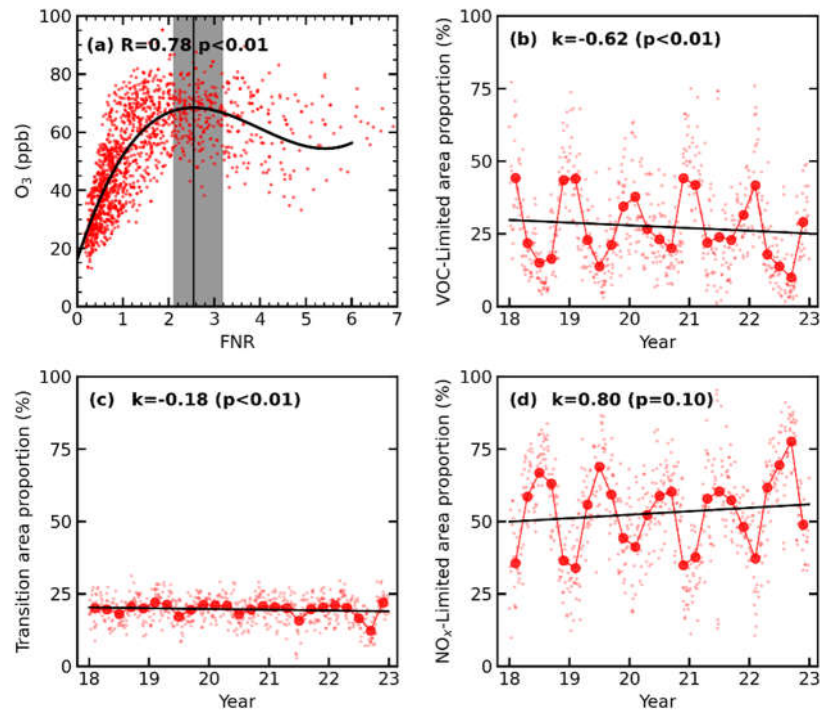


Fig.10. (a) Variation of monthly mean O_3 VMRs (~13:30) with monthly mean TROPOMI FNR in eastern China during May–September 2022. The solid line represents third–order polynomial fitting. The vertical line represents the maximum value of the fitted curve, and the vertical shadow represents the range of the curve slope from -3 to $+3$ (transition regime). Trends of TROPOMI observed area proportion for (b) VOC–limited regime, (c) Transition regime, and (c) NO_x –limited regime over eastern China during May–September 2018–2022. The light red dots in (b–d) represent the daily values, and the solid red dots are monthly mean values.

5

10

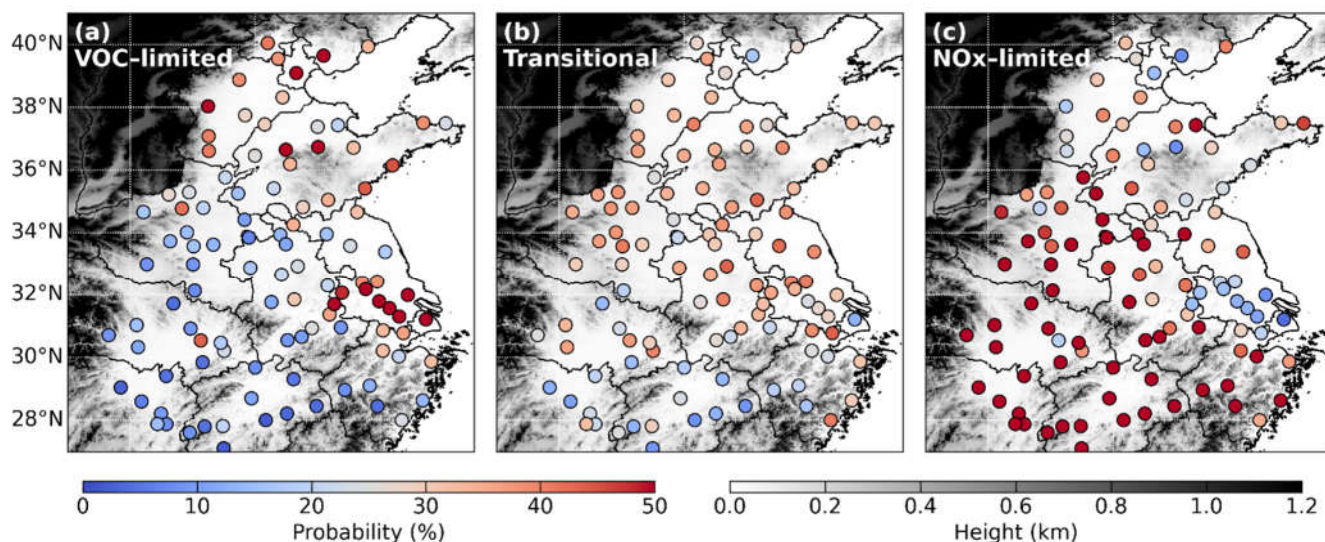


Fig.11. Occurrence probabilities of the (a) VOC-limited regime, (b) transition limited regime, and (c) NO_x -limited regime spatial distributions in eastern China derived by TROPOMI observations during May–September 2018–2022.

5

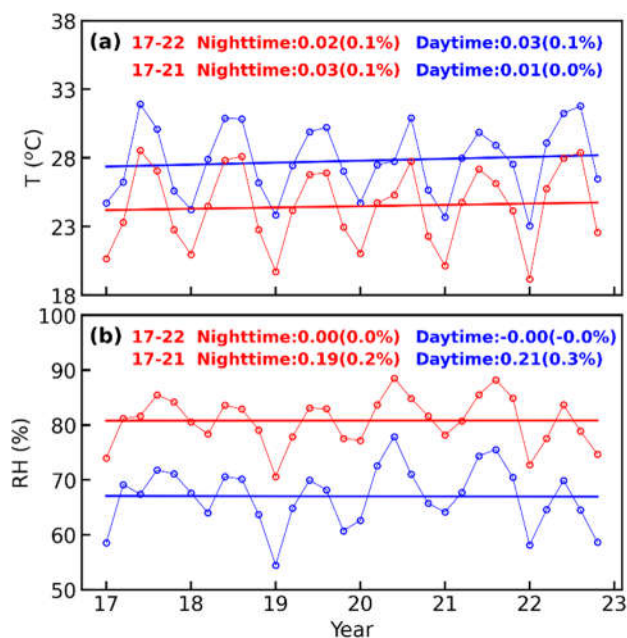


Fig.12. Daytime (7:00–19:00) and nighttime (19:00–07:00) (a) T and (b) RH trends in ERA5 reanalysis data in eastern China during May–September 2017–2022 and May–September 2017–2021. The labels at the top right of each panel represent the trend of T and RH in eastern China during May–September 2017–2022 and May–September 2017–2021.

10

Table 1. Observed, Meteorologically, and anthropogenically driven trends of 2% and 98% O₃ percentiles in eastern China from 2017 to 2022 and from 2017 to 2021.

	May–September 2017–2022 trends						May–September 2017–2021 trends					
	2%			98%			2%			98%		
	Obs.	Mete.	Anth.	Obs.	Mete.	Anth.	Obs.	Mete.	Anth.	Obs.	Mete.	Anth.
Total	0.115	0.008	0.107	-0.178	0.005	-0.183	0.027	-0.044	0.071	-0.363	-0.119	-0.244
May	0.322	0.017	0.305	-0.020	-0.661	0.641	-0.438	-0.257	-0.181	-3.702	-0.968	-2.734
June	0.205	-0.032	0.237	-4.437	-1.894	-2.543	-0.364	-0.169	-0.195	-2.645	0.124	-2.769
July	0.768	-0.177	0.945	-1.745	-1.100	-0.645	0.665	-0.247	0.912	-2.974	-2.370	-0.604
August	0.371	0.084	0.287	-0.687	-0.156	-0.531	-0.003	-0.260	0.257	-1.473	-0.908	-0.565
September	1.290	0.319	0.971	1.999	1.136	0.863	0.884	-0.126	1.010	1.352	0.814	0.538